

# The Zeldovich approximation: key to understanding Cosmic Web complexity

Johan Hidding\*, Sergei F. Shandarin<sup>†</sup> and Rien van de Weygaert\*

\* *Kapteyn Astronomical Institute, University of Groningen, Groningen, The Netherlands*

<sup>†</sup> *Department of Physics and Astronomy, University of Kansas, KS 66045, U.S.A.*

*emails: johannes.hidding@gmail.com; sergei@ku.edu; weygaert@astro.rug.nl*

Accepted 2013 November 4. Received 2013 November 2; in original form 2013 September 23

## ABSTRACT

We describe how the dynamics of cosmic structure formation defines the intricate geometric structure of the spine of the cosmic web. The Zel'dovich approximation is used to model the backbone of the cosmic web in terms of its singularity structure. The description by Arnold et al. (1982) in terms of catastrophe theory forms the basis of our analysis.

This two-dimensional analysis involves a profound assessment of the Lagrangian and Eulerian projections of the gravitationally evolving four-dimensional phase-space manifold. It involves the identification of the complete family of singularity classes, and the corresponding caustics that we see emerging as structure in Eulerian space evolves. In particular, as it is instrumental in outlining the spatial network of the cosmic web, we investigate the nature of spatial connections between these singularities.

The major finding of our study is that all singularities are located on a set of lines in Lagrangian space. All dynamical processes related to the caustics are concentrated near these lines. We demonstrate and discuss extensively how all 2D singularities are to be found on these lines. When mapping this spatial pattern of lines to Eulerian space, we find a growing connectedness between initially disjoint lines, resulting in a percolating network. In other words, the lines form the blueprint for the global geometric evolution of the cosmic web.

**Key words:** cosmology: theory, dark matter, large-scale structure, methods: analytical, numerical

## 1 INTRODUCTION

Over the last three decades, the study of the large-scale structure has thrived in both observations and theory. This was the consequence of the new insights obtained via large new galaxy redshift surveys, the tremendous increase of computing power, the related emergence and advances of computer simulations, and the development of new analysis methods and sophisticated theoretical models of gravitationally driven structure formation. However, while an overall theoretical framework for the emergence and evolution of the large scale structure of the universe has been gradually taking shape, there is not yet a com-

prehensive theory for the formation and evolution of the intricate and complex structure of the cosmic web.

### 1.1 Historical overview

Currently, there are a few approximate analytical models describing a range of features and characteristics of the cosmic web. It is in particular the theoretical framework of Bond, Kofman & Pogosyan (1996), responsible for coining the name "cosmic web", which has succeeded in combining the aspects of the anisotropic nature of gravitational collapse with the hierarchical nature of the process (for a review, see van de Weygaert & Bond 2008). It

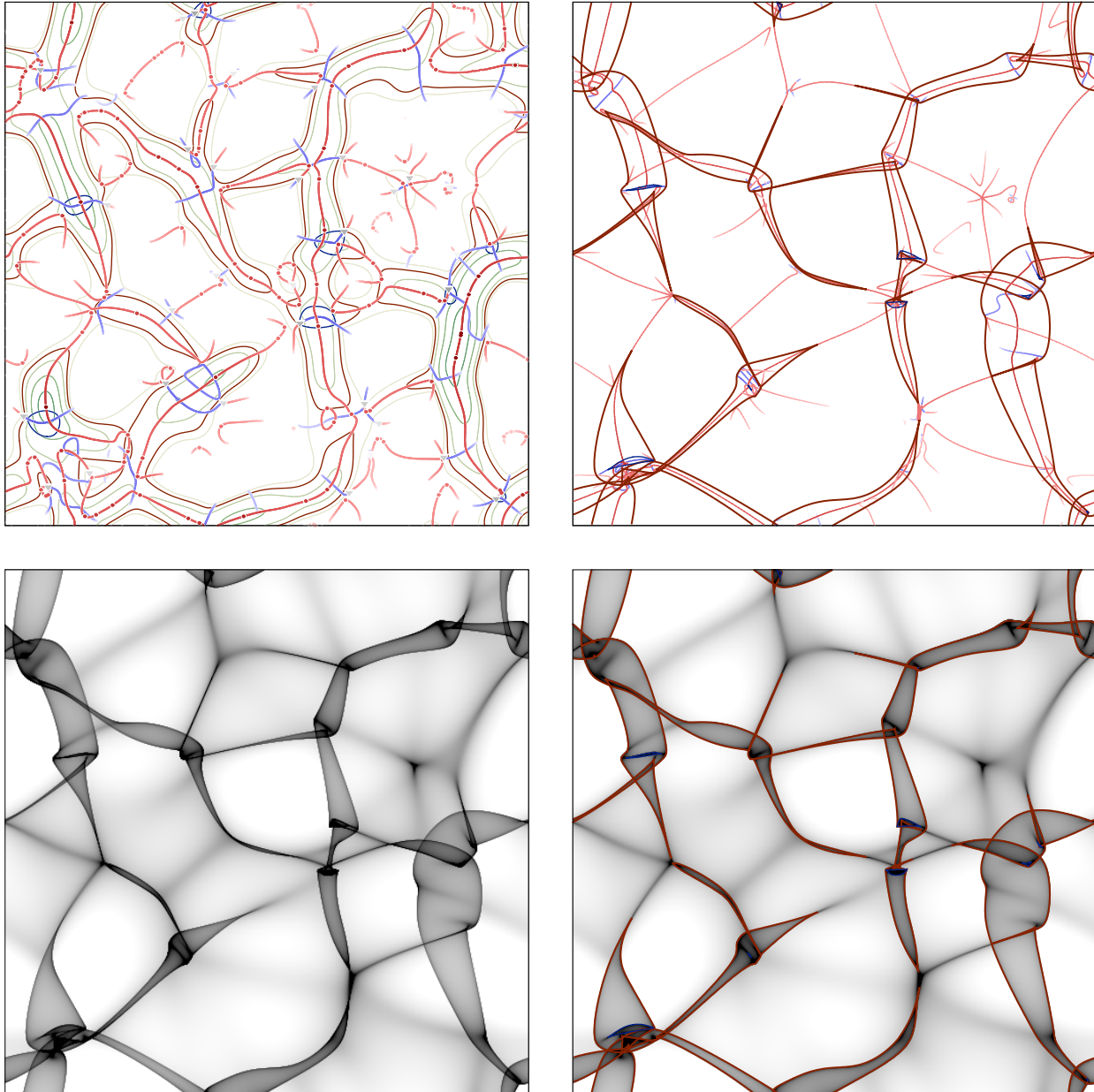


**Figure 1.** Zeldovich Approximation: Lagrangian & Eulerian Singularity Structure. First panel: the Lagrangian skeleton that we find using the method presented in this paper. In dark-red is the contour of the major eigenvalue corresponding to the time at which we plotted the Eulerian images that occupy the other three panels. Top-right panel: structural and singularity information from the first panel mapped to Eulerian space, as proscribed by the ZA. Bottom lefthand panel: density distribution in Eulerian space. Bottom righthand panel: density field in Eulerian space, with the singularity outline superimposed (red edges).

incorporates the statistics of peaks in primordial Gaussian fields Bardeen et al. (1986) with a sophisticated non-local description of the hierarchical evolution of peaks by means of the peak-patch formalism (Bond & Myers 1996a; Bond & Myers 1996b,c). The latter models the nonlinear anisotropic collapse by means of the homogeneous ellipsoid model (Lin, Mestel & Shu 1965; Icke 1972,

1973; White & Silk 1979), linking its linear stage to the Zel'dovich approximation (hereafter the ZA).

The former is supposed to work on small scales where density perturbations have reached the nonlinear stage of structure formation, while on large scales the density perturbations remain linear or quasilinear. The boundary separating the two approaches is defined by a heuristic

condition requiring that the multistream flows in the ZA involve only a small fraction of mass and thus can be neglected.

Zeldovich himself (1970) (see also Shandarin & Zel'dovich 1989) suggested to use the linear Lagrangian model until the multistream flows are well – but not overly – developed in the velocity field. The studies of Coles, Melott & Shandarin (1993) and Melott, Pellman & Shandarin (1994) showed that the ZA can be safely used on all scales down to the scale of nonlinearity,  $R_{nl}$ , defined by the condition  $\sigma_\delta(R_{nl}) \approx 1$ . By this stage most of pancakes have emerged, and still remain fairly thin. Up to this stage, the Zeldovich approximation describes conceptually correct, be it crudely, the emergence of multistream flow regions, caustics and the structural skeleton of the Cosmic Web (Doroshkevich, Ryabenskii & Shandarin 1973; Shandarin & Zel'dovich 1989; Buchert 1989, 1992; Coles, Melott & Shandarin 1993; Melott, Pellman & Shandarin 1994; Melott, Shandarin & Weinberg 1994; Coles & Sahni 1995; Melott, Buchert & Weiss 1995; Yoshisato, Matsubara & Morikawa 1998; Yoshisato, et al. 2006).

An additional prominent application of the Zeldovich approximation is that of its use as a tool for generating initial conditions in the simulations of cosmological structures (Doroshkevich, Ryabenskii & Shandarin 1973; Doroshkevich & Shandarin 1973; Doroshkevich, et al. 1980; Klypin & Shandarin 1983). Starting with these studies shortly after its inception, the Zeldovich approximation has become the major generator of the initial conditions in practically every cosmological N-body simulation since 1983. It also has been used in many theoretical studies of the non-perturbative nonlinear stage. However, its complete description and explanation of what it exactly predicts has not been provided yet. The first step in this direction was made twelve years after Zeldovich had published his paper. Arnold, Shandarin & Zeldovich (1982) described the topology of all generic singularities formed in the two-dimensional case and Arnold (1982, 1983) found the normal forms of all generic singularities in three dimensions. The two-dimensional study was focused mostly on the local properties of archetypical singularities while the global picture was described rather schematically. The authors obviously did not realize the computational complexity of the problem when promised to do a similar analysis in 3D in the following paper. However, impressive progress in computational geometry and computational graphics observed in the last couple of decades allows to hope for a significant step forward in understanding the geometry and topology of the structure in the ZA.

## 1.2 the Cosmic Skeleton

One of the major new results of this study is the demonstration that a particular set of lines and points in Lagrangian space form a progenitor of the skeleton of the

structure at the non-linear stage<sup>1</sup>. The first attempt to reduce the structure to a geometrical skeleton was done in the adhesion approximation (Gurbatov, Saichev & Shandarin 1989; Kofman, Pogosyan & Shandarin 1990; Gurbatov, Saichev & Shandarin 2012) (also see Hidding, van de Weygaert & Vegter (2013)). In the adhesion description, the skeleton was constructed from the linear gravitational potential by a geometrical procedure based on the approximate gravitational dynamics of the ZA. Later, Novikov, Colombi & Doré (2006) and Sousbie et al. (2008), as well as Aragón-Calvo et al. (2010), also discussed the skeleton or spine of the large-scale structure, be it in a rather different context. They constructed a skeleton from the known nonlinear density field on the basis of Morse-Smale theory. According to this description, the skeleton is traced by the separatrices that connect singularities in the density field. While the former derives the skeleton from the linear state by using gravitational dynamics as approximated by the ZA, the latter is purely a topological construction derived from the given density field.

Following a philosophy similar to that of our study, Pogosyan et al. (2009) followed up on the work by Sousbie et al. (2008) with a profound analysis of the critical lines in a density field. These were identified with those of the skeleton of the cosmic web. Our study sheds a different light on the skeleton of the cosmic web, by connecting it to the dynamical development of the density field. It accomplishes this by focussing on the linear deformation field in the primordial density field. Our study demonstrates that the spatial structure of the cosmic web, as it emerges out of the primordial universe, should be identified with critical lines in Lagrangian space. These lines mark the regions near which all decisive dynamical processes take place.

## 1.3 This paper

The principal incentive for our study is the identification of the spine of the dynamically evolving cosmic web in the primordial density field. We argue that this is entirely determined by the set of singularity lines, along which we may trace the caustics that form in the matter distribution as its phase-space structure attains an increasingly complex multistream character.

It is hardly feasible, or practical, to analyze the full nonlinear gravitationally evolved mass distribution such as modelled by cosmological N-body simulations. However, for our understanding of the geometric structure of the cosmic web we are greatly helped by the observation that the fundamental singularity and caustic structure of the cosmic web is basically entailed in the quasi-linear description of the Zeldovich approximation. Although the dynamics in the ZA is substantially simpler than that in cosmological N-body simulations, the ZA provides all the

<sup>1</sup> The skeleton becomes a set of surfaces, edges and vertices in 3D.

necessary concepts and language required for the analysis of the realistic dynamics of cosmological N-body simulations. It involves the concepts of phase space, Lagrangian submanifolds, multistream flows and caustics. This fact that the Zeldovich approximation combines its mathematical flexibility and simplicity with the full richness of concepts that we find in the more complex reality makes it unique among all theoretical models that seek to describe the structure and evolution of the cosmic web.

The main rationale behind our study is therefore that of an attempt to provide a comprehensive description of what the ZA actually predicts in terms of the dynamically evolving spine of the cosmic web. It may seem puzzling that in more than forty years after its inception, the ZA would still require further discussions and explanations. Instead of presenting another discussion of the accuracy of the Zeldovich approximation, this paper has the intention to reveal new interesting and useful aspects of the ZA and demonstrate that the seemingly simplistic mathematical form of the ZA harbours a rich geometry and complex topology for the emerging structures it describes.

There are a few characteristics of the ZA that makes its analysis and understanding drastically different and more difficult than that of linearly evolving spatial random fields. A first important aspect is that the evaluation of the Eulerian density field in the ZA requires both the deformation tensor and the displacement vector fields (see sect. 2). Eulerian linear theory only requires one scalar field, the initial density field. The geometry and topology of vector and tensor fields are considerably more complex than that of scalar fields (Tricoche 2002). An important second aspect is that of the stochastic properties of the eigenvalues of the deformation tensor field. Even when its individual components have a Gaussian distribution, the eigenvalues have a non-Gaussian distribution in all senses (Doroshkevich 1970): geometrical, topological and in terms of their probability distribution function. An additional major complication is related to the generation of multistream flows. This requires a nonlocal analysis. We will address these issues in far greater detail than previous studies have done.

In this study we restrict our analysis to the two-dimensional case. While it is considerably simpler than in 3D, the two-dimensional analysis still reveals many non-trivial features that also emerge in three dimensions. All basic concepts of two-dimensional theory remain the same in 3D, which renders the 2D analysis a useful and crucial step towards understanding the full three-dimensional case. The latter is the subject of an accompanying paper in preparation.

Aiming for the cosmological applications, we consider the evolution of a system consisting of collisionless particles interacting only via gravity and having an extremely low temperature. The examples of currently popular hypothetical dark matter particles are neutralinos and axions. For instance, if the mass of the universe is dominated by a weakly interacting massive particle with mass of 100 GeV, then there would be  $\sim 10^{67}$  such particles in the

Milky Way alone. This implies that the evolution of the dark matter distribution in the universe can be accurately described by a model of a cold collisionless continuous medium.

Reading this paper does not require previous knowledge of catastrophe theory or even the ZA. We provide a brief summary of the ZA in section 2, follow by an informal introduction to the theory of Lagrangian singularities in section 3. In the rest of the manuscript, we analyze the role of singularities in outlining the cosmic skeleton. Section 4 describes the role of every generic singularity in the Zeldovich approximation. Subsequently, in section 5 we explain how the cosmic web is assembled around the progenitor of the skeleton. Finally, in section 7 we summarize and discuss the major results.

## 2 THE ZEL'DOVICH APPROXIMATION

The Zeldovich approximation is particularly simple in comoving coordinates  $\mathbf{x} = \mathbf{r}/a(t)$ , where  $a(t)$  is the scale factor and  $\mathbf{r}$  are physical coordinates. It relates the initial Lagrangian coordinates  $\mathbf{q}$  at  $t \rightarrow 0$  and Eulerian coordinates  $\mathbf{x}$  at time  $t$  by an explicit relation

$$\mathbf{x}(\mathbf{q}, D_+(t)) = \mathbf{q} + D_+(t)\mathbf{s}(\mathbf{q}) \quad (1)$$

where the vector field  $\mathbf{s}(\mathbf{q})$  is determined by the initial density perturbations and  $D_+(t)$  is the linear density growth factor fully specified by the cosmological parameters. The Zeldovich approximation assumes that the initial displacement field  $\mathbf{s}(\mathbf{q})$  is a potential vector field,

$$\mathbf{s}(\mathbf{q}) = -\nabla_{\mathbf{q}}\Psi(\mathbf{q}), \quad (2)$$

in which the scalar displacement potential  $\Psi$  is directly proportional to the linearly extrapolated gravitational perturbation,

$$\Psi(\mathbf{q}) = \frac{2}{3Da^2H^2\Omega} \phi_{lin}(\mathbf{q}). \quad (3)$$

The potential character of the deformation vector is a direct consequence of the potential character of the growing mode of the gravitational instability in an expanding universe. An additionally important aspect of the Zeldovich approximation, reflecting its Lagrangian nature, is the deformation of mass elements. The deformation is specified by the deformation tensor,

$$d_{ij} = -\partial s_i / \partial q_j. \quad (4)$$

From equation (1) one may easily infer an explicit expression for the density as a function of Lagrangian coordinates and time. If we consider the conservation of mass in differential form,

$$\rho(\mathbf{x}, t)d\mathbf{x} = \bar{\rho}(t)d\mathbf{q}, \quad (5)$$

the density evolution directly follows from

$$\rho(\mathbf{x}, t) = \bar{\rho}(t) J \left[ \frac{\partial \mathbf{x}}{\partial \mathbf{q}} \right]^{-1}, \quad (6)$$



where  $J[\partial\mathbf{x}/\partial\mathbf{q}]$  is the Jacobian determinant of the map given by equation 1. It is convenient to write equation 6 in terms of the eigen values  $\lambda_i = (\alpha, \beta)$  of the deformation tensor  $d_{ij}$ ,

$$\rho(\mathbf{q}, t) = \frac{\bar{\rho}(t)}{(1 - D_+(t)\alpha(\mathbf{q}))(1 - D_+(t)\beta(\mathbf{q}))}, \quad (7)$$

where a commonly used ordering of the eigen values  $\alpha \geq \beta$  is assumed. On the basis of this equation, we may immediately infer two key features of structure formation described by the Zeldovich approximation. The first one is that the density becomes infinite as soon as  $D(t)\alpha = 1$  or  $D(t)\beta = 1$ . In addition, this collapse is nearly always anisotropic as in general the eigenvalues<sup>2</sup>  $\alpha \neq \beta$ .

It is easy to see that Eulerian linear perturbation theory (ELPT) is a limiting case of the ZA. Expanding the expression for the Lagrangian density (eqn. 7) in a Taylor series,

$$\rho(\mathbf{q}, t) = \bar{\rho}(t) + \bar{\rho}(t)D_+(t)(\alpha + \beta) + \dots, \quad (8)$$

clarifies the relation between the known linear expression for the density contrast,  $\delta_{lin}$ ,

$$\delta_{lin} := \frac{(\rho_{lin} - \bar{\rho})}{\bar{\rho}} = D_+(t)(\alpha + \beta). \quad (9)$$

Formally speaking, the ZA is valid only in the linear regime when both  $|D\alpha| \ll 1$  and  $|D\beta| \ll 1$ . However, Zeldovich made the bold prediction that it might be a good qualitative and arguably even a quantitative approximation up to the beginning of the nonlinear stage, i.e. up to the stage at which  $|D\alpha| \approx 1$ . Numerous studies confirmed the conjecture and elaborated on the quantitative accuracy and limitations of the approximation (Doroshkevich, Ryabenskii & Shandarin 1973; Shandarin & Zel'dovich 1989; Buchert 1992; Coles, Melott & Shandarin 1993; Melott, Pellman & Shandarin 1994; Melott, Shandarin & Weinberg 1994; Coles & Sahni 1995; Melott, Buchert & Weiss 1995; Yoshisato, Matsubara & Morikawa 1998; Yoshisato, et al. 2006, , also see references therein).

Technically speaking, the ZA is an extrapolation of Lagrangian linear perturbation theory (LLPT) beyond the range of its formal applicability. There are two fundamental differences of LLPT from its Eulerian counterpart ELPT. As may be inferred from equations 7 and 9, the calculation of the density LLPT uses the full deformation tensor while ELPT relies only on its trace. The second difference is due to the necessity in LLPT of mapping from Lagrangian to Eulerian space in order to evaluate the density field in Eulerian space. Even at small  $\sigma_\delta$ , where  $\delta = \Delta\rho/\bar{\rho}$ , the difference between LLPT and ELPT can be quite noticeable if the scale of the initial i.e. linear velocity field is considerably greater than that of density fluctuations (Peebles 1980). In this, we assume that  $\sigma_\delta$  is evaluated in ELPT. The difference between LLPT and ELPT becomes considerable when both are extrapolated

to a larger  $\sigma_\delta$ . A particularly obvious problem occurring in ELPT is the emergence of negative densities, i.e.  $\rho < 0$ , in regions with a large initial density deficit. For example, if ELPT is extrapolated to  $\sigma_\delta = 0.5$ , the regions with negative densities occupy approximately 2.3% of the volume. This fraction increases to almost 15% at  $\sigma_\delta = 1$ . Evidently, for a physical model this is an unacceptable circumstance. LLPT is completely free of this problem: at all times it predicts  $\rho > 0$ , regardless of the magnitude of  $\sigma_\delta$ .

Equation (1) encapsulates the mapping by the LLPT from Lagrangian space to Eulerian space. Its ramifications can be explored analytically before an overwhelming fraction of mass elements starts to experience shell crossing. The mathematical complications increase rapidly as the number and extent of the multistream flow regions proliferates. In particular interesting are those mass elements which are separated by finite distances in Lagrangian space and end up at the same places in Eulerian space. These caustics are key manifestations of the dynamically evolving mass distribution and mark the emerging cosmic web. To understand and assess this aspect of the Zeldovich approximation, we require numerical modeling, in particular for the cosmologically relevant situation of random initial conditions.

### 3 THEORY OF SINGULARITIES

Before we start our investigation of the spatial network defined by the Zeldovich approximation, we need an inventory of the individual singularities that may emerge as the cosmic mass distribution evolves into a weblike pattern. These singularities define the outline of the principal components of the cosmic web, while others arrange the spatial connections that line these components into a pervasive spatial network.

To be able to appreciate this structure, we need to build an inventory of the different caustic geometries that we encounter in the Zeldovich approximation. Having obtained insight into the character of the individual singularities, we will be equipped to appreciate their embedding in an extensive and more realistic network of structures.

For a complete inventory of all possible singularities we need to resort to the mathematical branch of catastrophe theory. In this section we will present a systematic, yet schematic, inventory of 2D singularities. While involving a complex mathematical formalism, within the limited context of the present study we invoke images to elucidate the key aspects of catastrophe theory and to appreciate the basic character of each singularity.

In the subsequent sections we will find how these caustic objects are the building stones of the evolving network of filaments and nodes.

<sup>2</sup> In this study we will demonstrate that the equality of the eigenvalues  $\alpha$  and  $\beta$  only occurs at isolated points.

### 3.1 Singularities and the Zeldovich approximation

When considering the displacement of mass elements from their Lagrangian location  $\mathbf{q}$  to their Eulerian position  $\mathbf{x}$ , according to the Zeldovich displacement equation 1, we may imagine this in terms of the Zel'dovich approximation outlining a (hyper)-surface in a four-dimensional *phase-space*. In this case, the four-dimensional phase-space  $(\mathbf{q}, \mathbf{x})$  is defined by four coordinates, the Eulerian space  $\mathbf{x}$  coordinates and the Lagrangian space  $\mathbf{q}$  coordinates. The hypersurface  $\mathbf{x}(\mathbf{q})$  is called a Lagrangian submanifold. Note that this definition of phase-space is different than the classic position-momentum phase-space. The non-dissipative nature of dark matter dynamics allows us to define a diffeomorphism (being a smooth and differentiable mapping that is both on-to and one-to-one) between these two concepts of phase-space throughout even the full non-linear dynamical evolution. In this mapping all the properties of the projection to Eulerian space are completely preserved.

The Lagrangian submanifold is a smooth single-valued function  $\mathbf{x}(\mathbf{q})$  of Lagrangian coordinates  $\mathbf{q}$ . While our brains are generally unable to imagine such a four-dimensional manifold, for the sake of insight we may illustrate some of the basic qualities for the equivalent situation of one-dimensional space, i.e. for the equivalent two-dimensional phase-space. This you may find in appendix A.

When looking at the evolving structure in the Universe, we are looking at the projection of the full four-dimensional submanifold on to Eulerian space  $\mathbf{x}$ . The evolving structure is a direct reflection of the changing geometry of the Lagrangian submanifold, in terms the gradual formation of folds in the submanifold and the orientation of the manifold. The folding is a direct manifestation of the emergence of multistream regions, where the local number of folds is determined by the number of streams at that location.

Locally, we may determine the resulting Eulerian density (perturbation)  $\delta(\mathbf{x}, t)$  by integrating over the various folds. If at location  $\mathbf{x}$  we find an  $N$  stream region, each corresponding to a solution  $\mathbf{q}^*$  for which  $\mathbf{x} = \mathbf{x}(\mathbf{q}^*, t)$ , the Eulerian density is

$$\delta(\mathbf{x}, t) + 1 = \sum_{\mathbf{x}=\mathbf{x}(\mathbf{q}^*, t)} \left| \det \left( \frac{\partial \mathbf{x}}{\partial \mathbf{q}} \right) \right|_{\mathbf{q}=\mathbf{q}^*}^{-1}. \quad (10)$$

where the sum is taken over all  $N$  solutions. It is in the projection of the four-dimensional Lagrangian submanifold that we find the appearance of singularities. These appear if one or more solutions  $\mathbf{q} = \mathbf{q}^*$  involve an accumulation of (Lagrangian) mass elements at the Eulerian location  $\mathbf{x}$ . This means that  $\det \left( \frac{\partial \mathbf{x}}{\partial \mathbf{q}} \right) = 0$ , implying an infinite local mass density,  $\delta(\mathbf{x}, t) = \infty$ .

The nature of the singularities that appear in the evolving cosmic mass distribution may vary. There is a limited number of different classes of singularities. These appear in different circumstances and configurations, and

$\nabla_{ij}f$	singularity
(- -)	maximum
(- +)	saddle
(+ +)	minimum

**Table 1.** Singularity character & Hessian eigenvalue signature

each play their role in outlining the spine of the cosmic web.

In the following subsections we will present a systematic census of the singularities that may emerge in the two-dimensional reality of the Zeldovich approximation. We will follow a mostly visual approach. After passing the basic mathematical concepts of Morse theory and catastrophe theory, we illustrate the various singularities and caustics as projections of a higher dimensional *phase-space* sheet onto Eulerian space.

### 3.2 Morse Theory

Catastrophe theory (Thom 1972; Zeeman 1977; Arnold 1992) describes how discrete events and objects emerge in a smoothly behaving system. It is built on Morse theory Milnor (1963).

Morse theory describes the general case of a - smooth and differentiable - function  $f(\mathbf{q})$ , in a mapping from  $\mathbb{R}^n$  to  $\mathbb{R}$ . Specific example of a Morse function are the heights of a mountain landscape, or the stochastic spatial random field defined by the mass distribution in the universe.

A key aspect of a Morse function  $f(\mathbf{q})$  is that at each location  $\mathbf{q}$  we can define its gradient,  $\nabla f$ . Within this gradient field, an exceptional and special position is taken by the *critical points*. These points are the ones where the derivative vanishes,  $\nabla f = 0$ . Singularities may have one of  $d + 1$  different identities. In the 2D situation we recognize three classes: maximum, saddle point and minimum. This identity is determined by the signature of the eigenvalues of the second derivative  $\nabla_{ij}f$  of the Morse function, following the listing in table 1.

The *critical points* play an essential role in determining the topology of a landscape. Considering the example of a cosmological density field, we may consider the density superlevel sets. These consist of the regions with a density superseding the defining threshold value and which have the corresponding density isocontour as boundary. As we lower the threshold value, the superlevel sets change topology as the threshold isocontour touches a *critical point*.

### 3.3 Catastrophes

Around its critical points, a Morse function may always be transformed into a quadratic form of local coordinates,

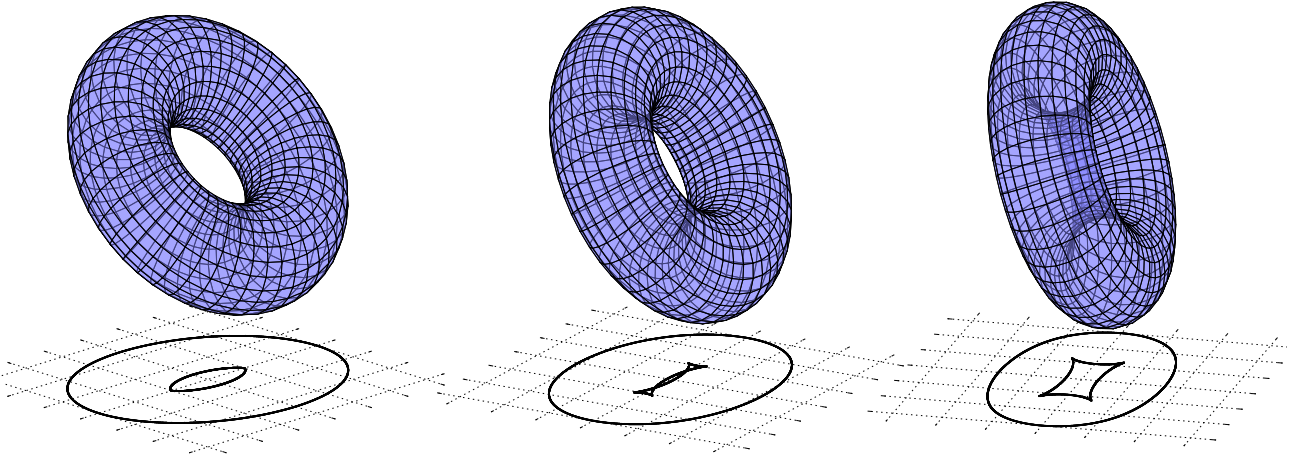


**Figure 2.** Caustic formation by projection. The figure illustrates how we may observe different caustics through the projection of a higher dimensional structure. The image shows a torus at different orientations in 3-D space. As we rotate the non-singular torus from a face-on to an edge-on view, we observe the changing morphology of the projection of the torus on the 2-D plane at the bottom of the figure panels change their morphology. In three snapshots, we show the metamorphosis of the resulting caustics. Left: instantaneous development of a caustic with two swallow-tail points ( $A_4$ ). Centre: splitting of central caustic into two cusps, a  $A_3$  singularity. Right: as the torus rotates further, the cusp points move to the edge.

following a transformation

$$\mathbf{q} = (q_1, q_2) \rightarrow (\xi_1, \xi_2), \quad (11)$$

for which

$$\zeta(\xi_1, \xi_2) = f(q_1, q_2) = \pm \xi_1^2 \pm \xi_2^2. \quad (12)$$

Any point for which the function cannot be transformed into such a *normal form* is degenerate. In general, the degeneracy of these points will disappear by expanding the function in a Taylor series in small perturbations of its parameters.

As the function becomes more complex and more parameters are needed for its description, a growing family of functions is generated. Most of these functions will not have degenerate points. However, at certain values of the parameters, degenerate points may appear. At these parameter values, the function will make a transition to new, very different behaviour. The parameter set with these values defines a bifurcation point, and these events are called *catastrophes* (Thom 1972; Zeeman 1977; Arnold 1992).

As more parameters are added, and the functions become more complex, the family of different types of catastrophes grows. Theory teaches us that there are only a few topologically different types of singularities possible, and that these are stable under perturbation (Thom 1972; Zeeman 1977; Arnold 1982, 1983). In this paper we will follow the ADE classification of catastrophes introduced by Arnold. The name reflects a deep connection of the theory of singularities with simple Lie groups. In total, five point-like singularities can be identified, the cusps  $A_3^+$  and  $A_3^-$ , the swallow tail  $A_4$ , and the umbilics  $D_4^+$  and  $D_4^-$ .

Within the context of the Zeldovich approximation, we are interested in the branch of catastrophe theory that deals with Lagrangian singularities. Given the observation that the limited family of possible singularities is stable under perturbation, we expect that the singularities identified in the ZA evolved mass distribution will also be present in the nonlinear case. Within the limited context of the present study, we restrict elucidation of its key aspects through visualization by means of images.

### 3.4 Planar torus projection: catastrophe by example

For the purpose of obtaining an intuitive appreciation of the situations in which singularities may appear, we may turn towards the illustration in figure 2. The image shows a torus at different orientations in 3-D space. As we rotate the non-singular torus from a face-on to an edge-on view, we observe the changing morphology of the projection of the torus - the black solid contour lines - on the plane at the bottom of the figure panels.

The planar projection is shown for three instances. The projection in the lefthand panel contains  $A_2$  and  $A_4$  singularities, while the central panel also contains  $A_3$  singularities. The simplest form of singularity is the fold singularity, the  $A_2$  singularity in Arnold's ADE classification. We observe it when we look right through the hole at the center of the torus. The structure seen in the lefthand panel emerges when the torus is tilted upward and at one particular instant passes through a stage where the center caustic assumes to swallow-tail points at its

name	ADE	$F(\mathbf{q})$ normal form	time
Cusp	$A_3$	$F(q_1) = q_1^4 + \lambda q_1^2$	$t = \pm\lambda \mp \tau^2$
creation	$A_3^+$	birth of a pancake	
annihilation	$A_3^-$	merger of two pancakes	
Swallowtail	$A_4$	$F(q_1) = q_1^5 + \lambda q_1^3 + \mu q_1^2$	$t = \pm\lambda$ .
branching of a pancake			
Umbilic	$D_4$	$F(q_1, q_2) = 3q_1^2 q_2 \pm q_2^3 + 3\lambda(q_1^2 \mp q_2^2)$	$t = \pm\lambda + x_1 + ax_2$ .
Pyramid (elliptic)	$D_4^-$	change in associated eigenvalue for three cusps	
Purse (hyperbolic)	$D_4^+$	swap of associated eigenvalue between cusp and fold	

**Table 2.** Possible catastrophe metamorphoses (or perestroikas) in the 2-dimensional Zeldovich approximation. These are the normal forms as given in Arnold (1983). The formulas give the potentials belonging to each normal form, for a time parameter  $t$ . Each normal form has one or more free parameters, represented by  $\tau$  and  $\mu$ . In the context of the singularities in the Zel'dovich approximation,  $\tau$  and  $\mu$  are identified with the Lagrangian coordinate  $q_2$ . The parameter  $\lambda$  inserts the time dependence into the normal form expressions.

edge. These are the  $A_4$  singularities. The central panel shows how these swallow tail singularities have split almost instantaneously into two cusps,  $A_3$  singularities. As we rotate this further, these move further outward (right-hand panel). The accompanying loss of two crosspoints by the central caustic is the result of a global change in the projection, and cannot be predicted from local considerations.

Although the illustration provides us with some visual intuition of the character and nature of singularities, we should also note that the configuration of a static and robust torus is not really representative for the situation we are addressing in this study. Within the context of the evolving cosmic mass distribution, we will study the projection of the Lagrangian submanifold. A direct manifestation of the dynamical evolution of the cosmic mass distribution is that this four-dimensional manifold itself is continuously changing, and it is the corresponding evolution of the manifold's projection that will result in the emergence of singularities.

### 3.5 Normal forms

To formalize our understanding of the different singularities, we describe them in terms of a *normal form*. Loosely speaking, a *normal form* may be defined as the minimal or simplest polynomial that captures the topology of a singularity. The normal forms represent a complete description of each singularity: via a transformation each stable singularity can be smoothly transformed into one of the normal forms.

We may formalize the concept through the definition of a corresponding family of potential functions,  $F_\mu(\mathbf{q})$ . The manifold  $\mathbf{x}(\mathbf{q})$ , i.e. the Eulerian position, is the gradient of the potential function,

$$\mathbf{x} = \mathbf{x}(\mathbf{q}) = \nabla_{\mathbf{q}} F. \quad (13)$$

The potential function is parameterized by  $\mu$ . These are a set of parameters that smoothly change as a function of

space or time. For example, in the context of the Zeldovich approximation the displacement field,  $\mathbf{x} = \mathbf{q} + D_+ \nabla_{\mathbf{q}} \phi_{\text{lin}}$ , can be related to the potential function,

$$F(\mathbf{q}) = \frac{\mathbf{q}^2}{2} + D_+ \phi_{\text{lin}}(\mathbf{q}). \quad (14)$$

The linear density growth factor  $D_+$  functions as a parameter. This expression establishes the link between the ZA and its formulation in terms of a normal form.

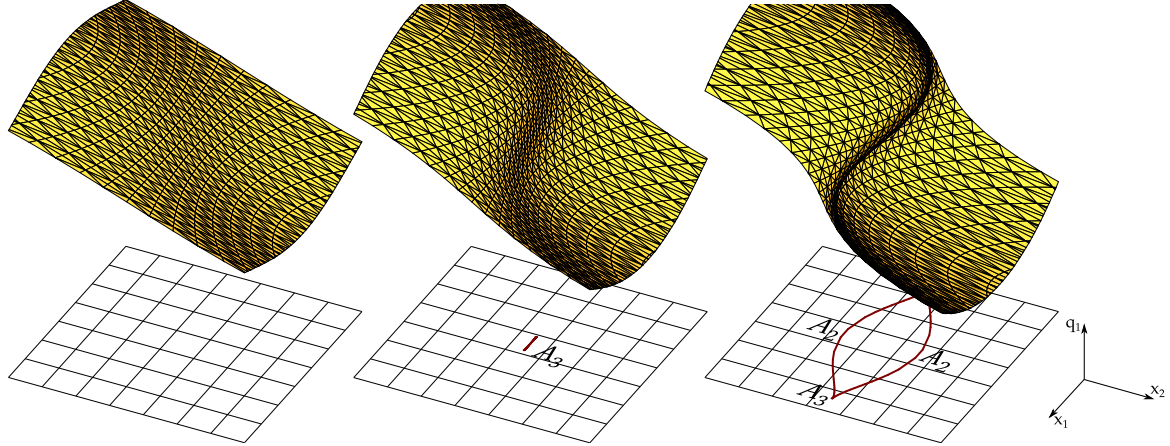
For understanding the topology and geometry of a singularity, the first derivative of the potential function  $F_\mu(\mathbf{q})$  is not particularly interesting. Via a trivial translation, the first order derivative may be transformed away. It are the higher order derivatives of the potential function  $F_\mu(\mathbf{q})$  which determine the type of a catastrophe.

From Morse theory we know that the critical points of the phase-space manifold  $\mathbf{x}(\mathbf{q})$  are the locations at which the first derivative of the surface  $\mathbf{x}(\mathbf{q})$ , and hence the second derivative of  $F_\mu(\mathbf{q})$ , is zero. Via a Taylor expansion we may study the local potential function at every Lagrangian point  $\mathbf{q}$  in the domain around these critical points. In the literature, these local functions are called the *germs* of the catastrophe geometries.

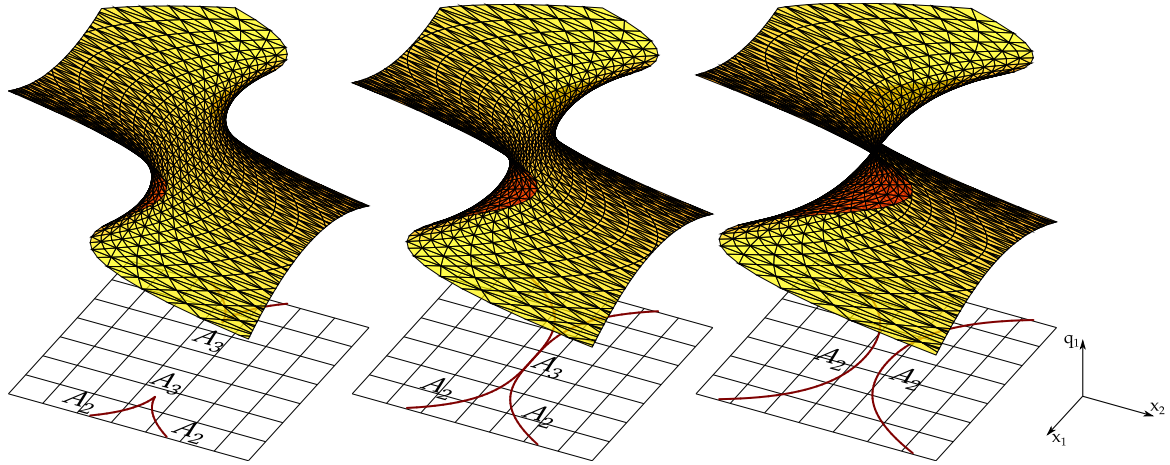
By means of a suitable coordinate transformation, we may subsequently - without any loss of generality - write the local potential functions  $F(\mathbf{q})$  in one of the normal form expressions given by Arnold (Arnold 1983) (see table 2). Following this formalism, we may identify any of the catastrophes found in the ZA modelled mass distribution with one of the basic catastrophe classes.

### 3.6 Inventory of 2-D singularities

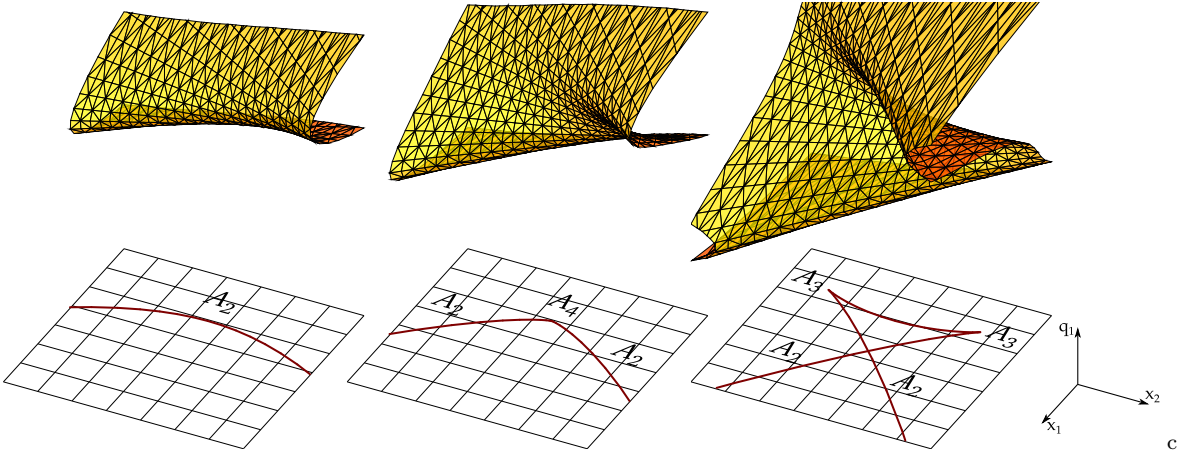
In the following subsections, we provide an inventory of illustrations of each of the fundamental singularities. To this end, figure 3 until figure 4 present impressions of evolving three-dimensional projections of the evolving phase-space manifold  $(\mathbf{q}, \mathbf{x})$  in the vicinity of the five fundamental classes of 2-D catastrophes listed in table 2. The



(a)  $A_3^+$ , the birth of a pancake. The linear term in the surface counters the cubic term, generating the singularity when the magnitude of their derivatives matches. This linear term grows with time, faster in the middle.



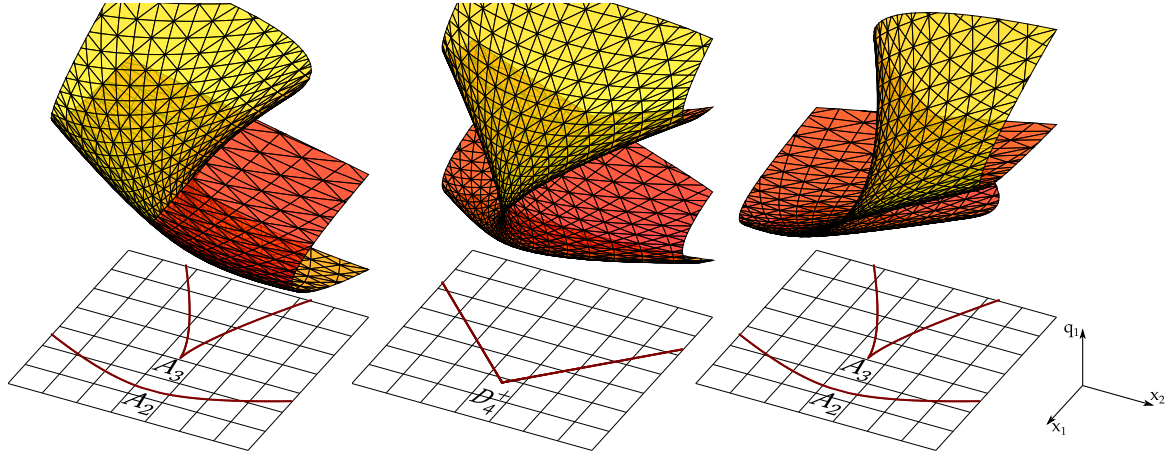
(b)  $A_3^-$  singularity and the merging of two pancakes. The linear term in surface has a minimum in the middle. So this is where the surface tangent goes singular last, joining the two three-stream regions that are already present.



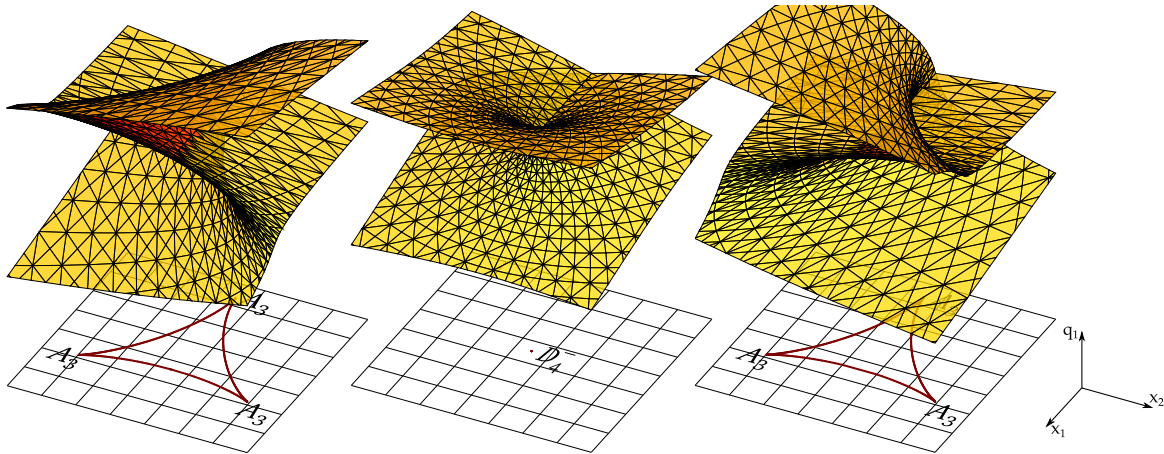
(c) The  $A_4$  swallow-tail singularity and the folding of a pancake. In the first image we see the edge of a pancake. This pancake develops a singularity, that then unfolds into two cusps moving away from each other.

**Figure 3.** A-series of singularities. The figures shows the 3D projection of the Euler-Lagrange phase-space sheet on to the configuration space  $(x_1, x_2, q_1)$ , with  $q_1$  along the vertical direction and the Eulerian plane  $(x_1, x_2)$  in the horizontal direction. The smooth yellow surface is the 3D projection of the phase-space sheet. Each singularity is shown at three different timesteps. Each image shows the phase-space sheet at one particular instant, along with the caustic structure - the black solid lines - in the 2-D projection on the Eulerian  $(x_1, x_2)$  plane. Although the images are rather schematic, these illustrations are fully representative for the general case that we encounter in the evolving cosmic mass distribution.





(a) The  $D_4^+$  singularity: the hyperbolic umbilic. The structure of this singularity cannot be embedded in 3D without having self-intersecting surfaces. Note that the center image shows a symmetric surface, but the deprojection of it resembles an earlier (or later) stage of development. The projection of two folds coincides. This will always happen locally at a  $D_4^+$  point. Thom (1969) called this singularity a 'purse'.



(b) The  $D_4^-$  singularity: the elliptic umbilic. This singularity produces the steepest density profile possible in 2D. Thom (1969) called this singularity a 'pyramid'.

**Figure 4.** The D-series of singularities, limited to the  $D_4$  singularities. The figures show the 3D projection of the Euler-Lagrange phase-space sheet on to the configuration space  $(x_1, x_2, q_1)$ , with  $q_1$  along the vertical direction and the Eulerian plane  $(x_1, x_2)$  in the horizontal direction. The smooth yellow surface is the 3D projection of the phase-space sheet. Each singularity is shown at three different timesteps. Each image shows the phase-space sheet at one particular instant, along with the caustic structure - the black solid lines - in the 2-D projection on the Eulerian  $(x_1, x_2)$  plane. Although the images are rather schematic, these illustrations are fully representative for the general case that we encounter in the evolving cosmic mass distribution.

table 2 lists the normal forms of these catastrophes following the formulation given by Arnold (1983). For a more formal description of the table's content, we refer to the next subsection 3.7

The images are based on the corresponding normal forms from table 2. For practical considerations<sup>3</sup>, we have to limit ourselves to showing a lower-dimensional projection of the phase-space sheet. The figures therefore depict the singularities in the form of three-dimensional pro-

jections of the Euler-Lagrange phase-space sheet on to the configuration space  $(x_1, x_2, q_1)$ , consisting of one Lagrangian coordinate - along the vertical direction - and two Eulerian coordinates along the horizontal plane. This projection of the phase-space sheet is the smooth yellow surface.

Each singularity is shown at three different timesteps, such that a row of three images shows evolution of the phase-space sheet along with the emergence of the caustic structure in the 2-D projection on the Eulerian  $(x_1, x_2)$  plane. A caustic appears where the phase-space sheet is perpendicular to the Eulerian plane  $E$ . Although the images are rather schematic, these illustrations are fully rep-

<sup>3</sup> Taking into account, as we stated above, that the human brain is not equipped for processing four-dimensional images.

representative for the general case that we will encounter in the evolving cosmic mass distribution.

### 3.6.1 A-series: folds, cusps and swallow-tails

Figure 3 shows the 3D phase-space sheet projections around the  $A_3^+$  (top row),  $A_3^-$  (central row) and  $A_4$  (bottom row), each with a sequence of three timesteps.

A *fold* is the edge of a pancake. As we can see in figure 3a, the first pancakes form at  $A_3^+$  points. They are the transient state where two *cusps* are created. Figure 3b shows how two cusps can meet to merge into two pancakes.

The two operations of cusp creation and annihilation will only build a network of filaments if there is a way to split a pancake. Figure 3c shows how this happens in the transient  $A_4$  singularity. We see how the edge of a pancake develops a ‘kink’<sup>4</sup>, which immediately bifurcates into two cusps showing the characteristic ‘swallow-tail’ pattern (hence the name). In practice, one of these cusps will join another pancake, thereby forming a tripod structure (see figure 15). The subsequent evolution depends on the surrounding environment, and is explained in section 4.

### 3.6.2 D-series: purses and pyramids

The most complicated type of singularities are the *umbilics*, or  $D_4$  singularities. In terms of the deformation tensor there is a  $D_4$  singularity if two eigenvalues are equal. They are presented in figure 3. The  $D_4$  singularity involves two types,  $D_4^+$  and  $D_4^-$ . They are shown in figures 4a and 4b respectively.

In the  $D_4^+$  case, the cusp corresponding to the second eigenvalue meets with the fold corresponding to the largest eigenvalue at the middle panel for one instant. The cusp then becomes a fold, and the fold becomes a cusp.

In the  $D_4^-$  case a curvilinear caustic triangle corresponding to the largest eigen value collapses in the middle panel of figure 4b. At the same instant, a similar triangle corresponding to the lowest eigenvalue emerges. This can be seen in the right panel.

Among all singularities in 2D, both types of  $D_4$  result in the highest concentration of mass. Note that the figures seem to show self-intersecting surfaces. This is an artefact of the lower-dimensional projection of the phase-space sheet. If we were to present them in 4D, we would see this that is no longer the case.

## 3.7 Lagrangian submanifold geometry and Arnold’s catastrophe formulation.

With respect to the geometry of the catastrophes, and the corresponding phase-space Lagrangian submanifold in

<sup>4</sup> one is tempted to say ‘cusp’, but that would be technically wrong

four-dimensional phase-space  $(\mathbf{q}, \mathbf{x})$ , we should add a few explanatory remarks with respect to normal form formulation listed in table 2.

The geometric structure of the catastrophes live in the Eulerian-Lagrangian phase-space  $E \times L$ . For a potential  $F(\mathbf{q}, t)$ , we may define the Lagrangian submanifold as the implicit surface

$$M(t) = \left\{ (\mathbf{x}, \mathbf{q}) \in E \times L \mid \mathbf{x} = \nabla F(\mathbf{q}, t) \right\}.$$

In the projection of  $M(t)$  on to Eulerian space  $E$ , we find caustics  $M_c \subset M$  at those places where the surface  $M$  is perpendicular to  $E$ . We may parameterize the submanifold by means of the vanishing determinant of the Hessian of  $F$ ,

$$M_c(t) = \left\{ (\mathbf{x}, \mathbf{q}) \in M(t) \mid \det \mathcal{H}(F) = 0 \right\}$$

At any time  $t$ , this gives us a set of caustic curves. Over a span of time these curves trace a surface called the *big caustic* (Arnold 1983).

To infer the time evolution from the big caustic, we need to define a second surface intersecting the big caustic. In general this results in a set of curves. It is the parametrisation of this surface that is given in the last column of table 2. It allows us to get both cusp creation and annihilation behaviour from a single definition of the big caustic.

The general formulation includes a few extra parameters. To arrive at the results in figure 3, the remaining parameter  $\tau$  may be identified with  $q_2$ . Following the same procedure for the case of the swallow tail catastrophe, in addition to the substitution of the time parameterization, we are still left with the free parameter  $\mu$ . We identified  $\mu$  with the remaining Lagrangian coordinate  $q_2$  to arrive at the result in figure 3c.

## 4 ZELDOVICH GEOMETRY: GENERIC SINGULARITIES AS PRINCIPAL ELEMENTS

The normal forms discussed in the previous section provide a useful and insightful guide to the local topology of individual singularities. However, the geometric structure emerging from the gravitational evolution of the random primordial conditions is far more complex. Different types of singularities emerge in a variety of combinations.

In this section we extend the image of the individual singularities to more generic circumstances. We will find how this involves different types of caustics, the conditions and environment in which they arise, and how these different caustic singularities connect into a pervading geometric network. The identification of the different classes of singularities and caustics within their generic cosmological context will form the basis for the development of a full geometric understanding of the way in which the Zeldovich approximation outlines the weblike spine of the Megaparsec scale matter distribution.

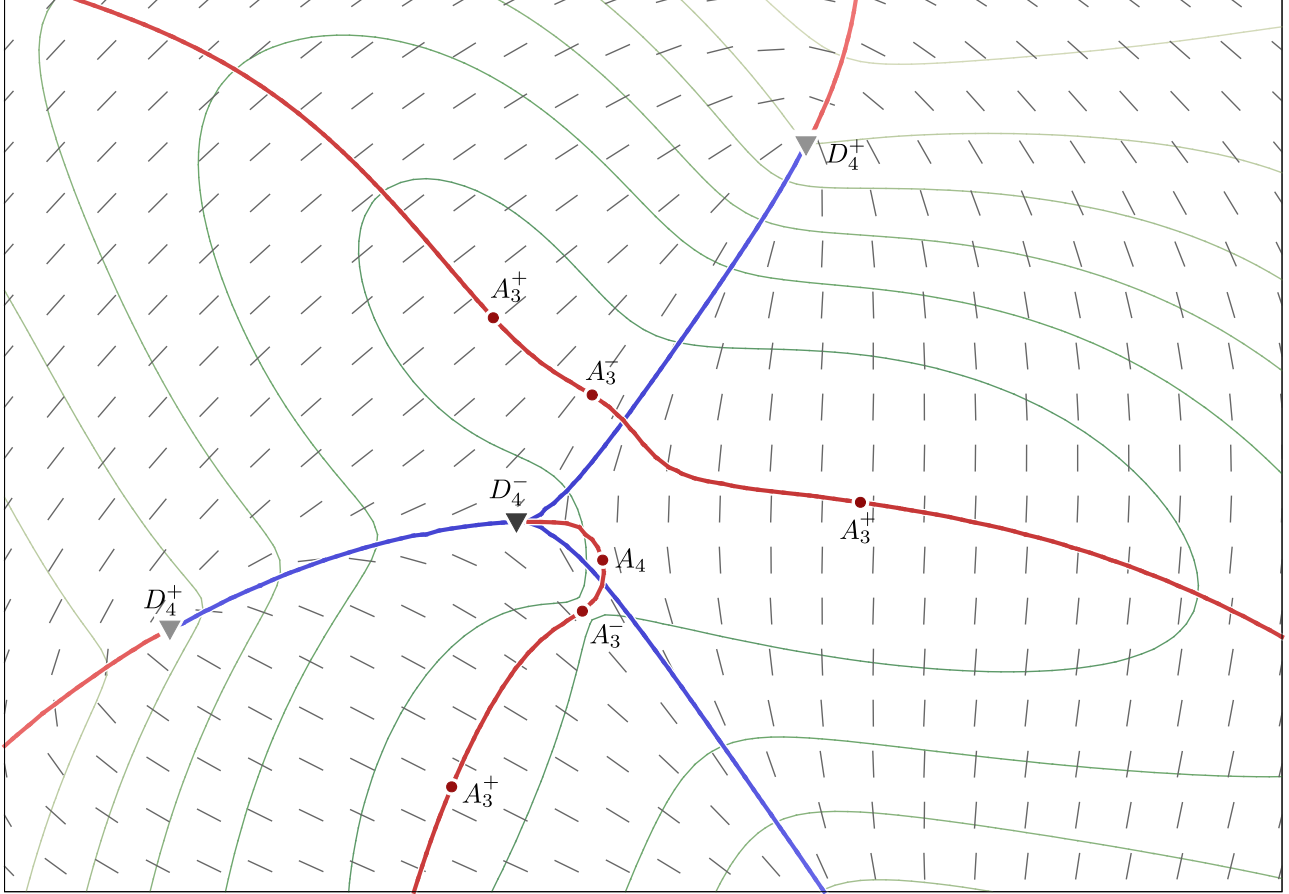


**Figure 5.** Deformation field: a Lagrangian visualisation. The contours show the value of the largest eigenvalue and the segments the direction of the corresponding eigenvector. The thick lines are the  $A_3$  lines that track the development of the caustics through time, red belonging to the first eigenvalue, blue to the second. Note that the  $A_3$  lines trace the places where the eigenvector is tangent to the contour. The maxima and minima of the eigenvalues also lie on such a line, denoted by  $A_3^+$  and  $A_3^-$  respectively. At the  $A_4$  point the  $A_3$  line has a local maximum, and the line is tangent to the contour of the eigenvalue. The  $A_3$  line terminates in a  $D_4$  point, continuing as an  $A_3$  line of the second eigenvalue. There are two types of  $D_4$  points, more about that is explained in section 4.6. Note: there is a tiny loop of the  $A_3^+$  line (red) covered by  $D_4^-$  symbol; two generic structures of  $D_4$  are plotted in figure 12 and an additional explanation is given in Appendix B

In most examples in the following subsections, we select - by eye - the simplest possible realizations out of a larger field realization. The singularities in these situations are usually located in relatively isolated environments. Singularities of other types are far removed from these locations. This usually involves rather artificial situations. In more generic (random) primordial conditions the singularities typically emerge in groups. These groups tend to exist of various types of singularities, generally clustered and at relatively close distances to each other. One particular illustration of the latter is figure 14, which shows an example where almost all kinds of singularities are packed in a small region.

#### 4.1 Caustics and the deformation field

The two-dimensional version of the cosmic mass distribution evolving according to the Zeldovich approximation is equivalent to that encountered in geometric optics (see e.g. Zel'dovich, Mamaev & Shandarin 1983). The most prominent aspect is that of the anisotropy of the collapsing structures and the resulting caustic structure, a direct reflection of the fact that in general the deformation tensor eigenvalues  $\alpha \neq \beta$ .

While it represents a complete and correct description of the patterns encountered in optics, the predicted structure is only an approximation of the structure forming in a gravitating medium. This was of course recognized by Zeldovich himself. In this respect, one might argue that the ZA becomes qualitatively incorrect when a significant fraction of mass experiences turns inside out more than two times in 2D, or three times in 3D.



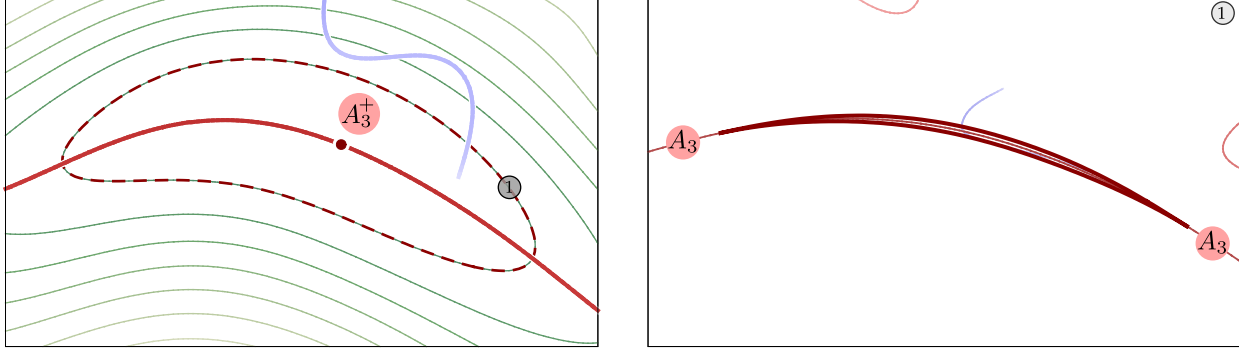


**Figure 6.**  $A_3$  cusp singularities and related  $A_2$  folds. Left panel: the progenitor of the caustic in Lagrangian space – red dashed line with label '1',  $A_3$  – thick red line, a maximum of  $\alpha$  – a red dot next to  $A_3^+$  label. Right panel: an  $\alpha$ -caustic in Eulerian space with two cusps marked as  $A_3$ .

To locate singularities in a generic situation, we need to study the deformation tensor

$$d_{ij} := -\frac{\partial s_i}{\partial q_j}, \quad (15)$$

of the displacement field

$$\mathbf{s}(\mathbf{q}, t) = \mathbf{x}(\mathbf{q}, t) - \mathbf{q}, \quad (16)$$

In the ZA, the displacement vector is factorized in a temporal and a spatial part,

$$\mathbf{s}(\mathbf{q}, D_+(t)) = D_+ \mathbf{s}(\mathbf{q}). \quad (17)$$

As long as the growth of structure is linear or quasi-linear, we may assume that the flow is a potential flow,  $\mathbf{s} = -\nabla_{\mathbf{q}}\phi_{\text{lin}}$ . In this situation, the deformation tensor will be symmetric. Our discussion of caustic formation is based on this situation and therefore remains valid into the nonlinear flows, for as long as the flow remains vorticity free.

The study of singularities in the displacement field is based on the characteristics of the deformation tensor field: critical points in the displacement field correspond to zero points in the deformation tensor  $d_{ij}$ . For obtaining insight into the nature and position of critical points, the most instructive approach is to focus on the study of the deformation field in terms of its eigenvalue fields  $\alpha(\mathbf{q})$  and  $\beta(\mathbf{q})$ , and the corresponding eigenvector fields. These fields completely characterize the deformation field, without loss of generality: the nature of the critical points is dependent on the signature of the eigenvalues  $\alpha$  and  $\beta$ . Important to note is that, by definition, we order the eigenvalues such that  $\alpha > \beta$ .

For appreciating the Lagrangian basis of our study, figure 5 illustrates the spatial distribution, in a Lagrangian volume, of the  $\alpha$ -component of the deformation field. For a specific realization of a random initial field we have depicted the  $\alpha$  isocontours as thin lines. In the same figure, we have indicated the (normalized) eigenvectors  $\mathbf{n}^\alpha$  of the  $\alpha$  eigenvalue field. They are depicted by means of line segments that are aligned along the direction of

the eigenvectors. Also, the figure indicates the location of special lines and points - singularities - that will be the subject of extensive discussion in later subsections. These play a key role in defining the skeleton of the cosmic web.

The ultimate fate of mass elements  $\mathbf{q}$  depends on the signature of the eigenvalues  $\alpha(\mathbf{q})$  and  $\beta(\mathbf{q})$ . As may be immediately inferred from the Zeldovich approximation (cf. eqn. 7, mass elements for which both eigenvalues  $\alpha$  and  $\beta$  are negative never reach a singularity. Those which have only one positive eigenvalue pass through a singularity once, while the ones with two positive eigenvalues do this twice. When it passes through a singularity, a mass element is turned inside out along the direction of the eigenvector.

By definition, structure in the universe is the result of a collective response of groups of mass elements to the gravitational force field responsible for the displacement of mass. In order to understand the spatial patterns in the evolving mass distribution, we therefore should not only concentrate on individual singularities, but also on their surroundings and on the complexes in which they are embedded. In the following subsections, we will seek to identify the spatial setting and grouping of the different classes of singularities that were identified in section 3.

## 4.2 $A_2$ lines & pancakes

It is not hard to see that if the evolution of the system starts from smooth initial condition, the location where collapse starts first are those around the maxima of  $\alpha(\mathbf{q})$  in Lagrangian space. These are the  $A_3^+$  points in the field, which in figure. 5 have been marked accordingly. The nature of these singularities will be discussed in more detail in the next subsection.

The subsequent evolution of cosmic structure consists of a gradual progression of Lagrangian regions experiencing collapse. At any given cosmic time  $t$ , these regions consist of the points on the isolines  $\alpha(\mathbf{q}) = 1/D(t)$  or  $\beta(\mathbf{q}) = 1/D(t)$ . In Lagrangian space, they form a set of lines,  $A_2^\alpha$  and  $A_2^\beta$ . The  $A_2^\alpha$  lines are the isocontours of the

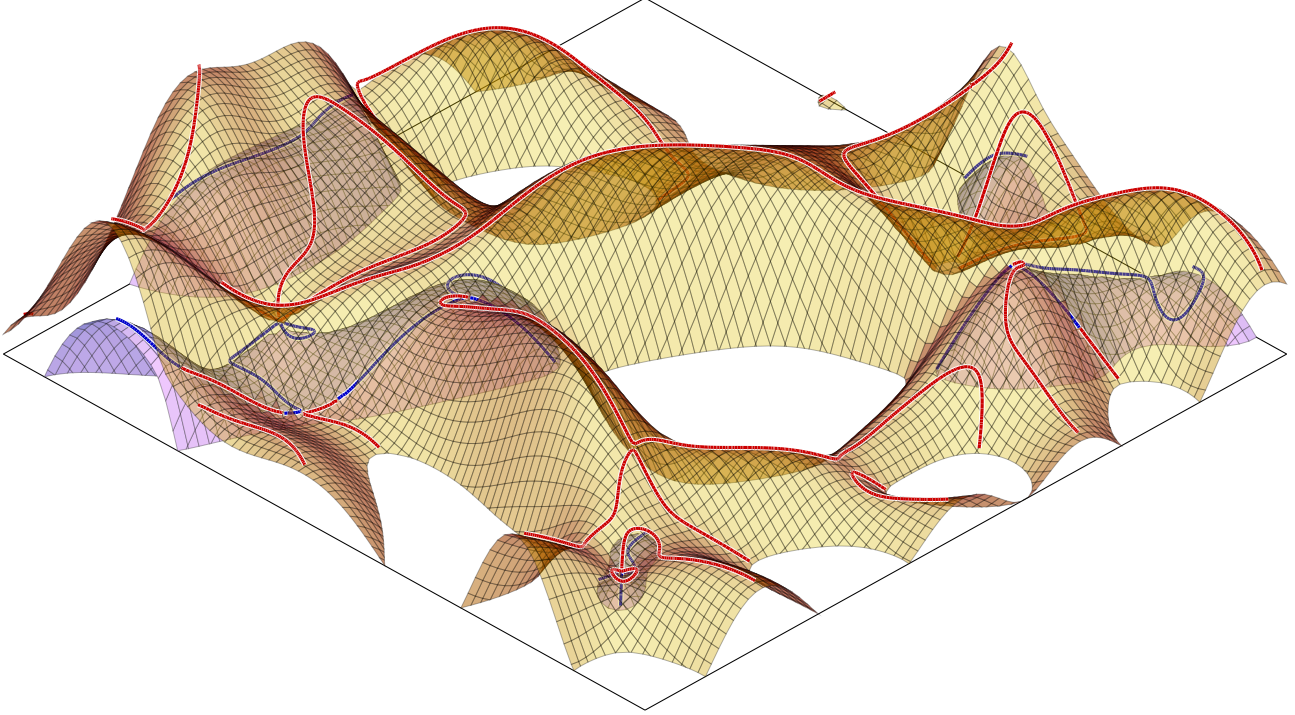


**Figure 7.**  $A_3$  lines and the eigenvalue landscape. The landscape of the eigenvalues  $\alpha$  and  $\beta$  of the deformation tensor is shown for values above a threshold value. The brown landscape concerns the field of  $\alpha$  values within a certain region of space. The blue landscape shows the run of the second eigenvalue in the same region of space, as far as the value of  $\beta$  is higher than the threshold. The  $A_3^\alpha$  lines are indicated as thick red lines, the  $A_3^\beta$  lines as blue lines.

eigenvalue  $\alpha(\mathbf{q}) = 1/D(t)$  or, in other terms, its eigenvalue level set.

Points residing on an  $A_2^\alpha$  line pass through an  $A_2$  fold singularity (see fig. 6). When they are mapped to Eulerian space we see them emerge as caustics. In the mapping from Lagrangian to Eulerian space, the lower edge of the  $A_2$  line is mapped into the upper caustic, while the upper edge moves towards the lower caustic (fig. 6). As the matter streams in and around the  $A_2$  contour cross each other's path. The resulting pancake region demarcates a three-stream region, enclosed by the *fold* caustics. At any location within its interior we find three velocities, each corresponding with one of the streams. In such multistream regions, mass elements of a different origin are crossing each other. One of the streams in the pancake region corresponds to fluid elements that have already experienced a singular collapse along the direction of the eigenvector  $\mathbf{n}^\alpha$ . We refer to appendix (A) for a discussion of the more transparent equivalent one-dimensional situation.

The two families of emerging caustics are called  $\alpha$ - and  $\beta$ -caustics, while the corresponding isocontours in Lagrangian space will be referred to as *progenitors of caustics*. Because nearly all properties of  $\alpha$ - and  $\beta$ -caustics are equivalent, in order to prevent unnecessary repetitions we refer to both by means of  $\lambda$ , which may either mean  $\alpha$  or  $\beta$ .

The resulting image is one in which the  $A_3^+$  points are the buds of the emerging cosmic structure. At their Eulerian locations we observe the first stages of the formation of the cosmic web. Subsequently, we witness a gradual progression of  $\alpha$  isocontours attaining the state of  $A_2^\alpha$  line. As this happens, in Eulerian space we see the expansion of the corresponding *fold* caustics.

### 4.3 $A_3$ -lines: progenitors of cusps

A key element for our understanding of spatial pattern formation in the Zeldovich approximation is that of the  $A_3$ -lines in Lagrangian space. The  $A_3$  lines in the Lagrangian deformation tensor field form the backbone of the emerging structure: they are the progenitors of the cosmic skeleton in Eulerian space. To develop one's intuition for the spatial context and significance of  $A_3$  lines with respect to the underlying deformation field, figure 7 depicts a 3D impression of the outline of the  $A_3$  paths along the crests and slopes of the eigenvalue  $\alpha$  (and  $\beta$ ) landscape. The height of this landscape also depicts the time at which the local mass element collapses. At any single instance of time the mass element where the  $\lambda$ -contour and  $A_3$ -line cross, corresponds to a point in Eulerian space where we can find a cusp singularity. As time progresses, and the  $\lambda$ -contour descends on the landscape, the cusps travel outward along the  $A_3$ -lines. In this manner the  $A_3$ -

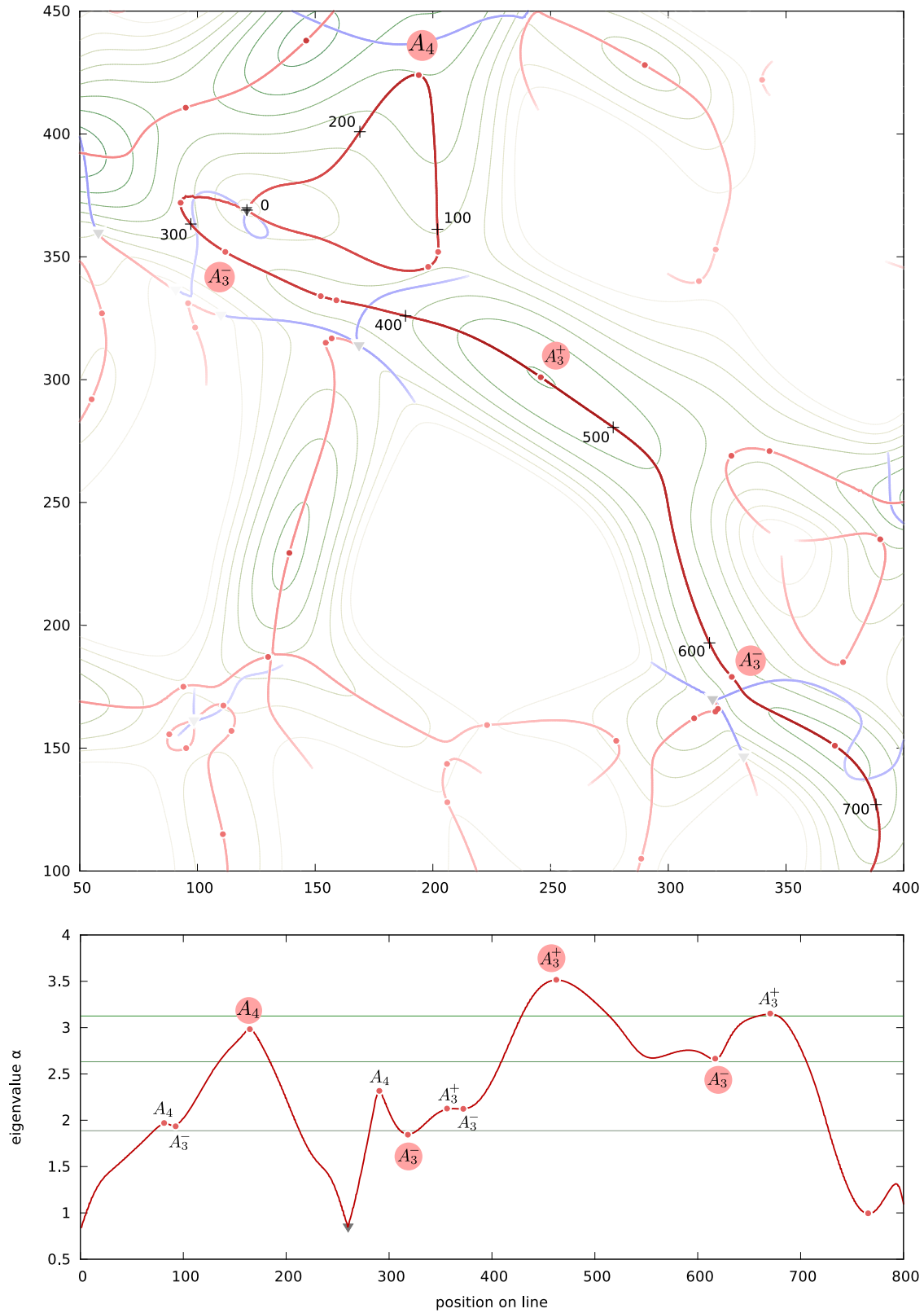


**Figure 8.**  $A_3$  eigenvalue profile. The profile of the first eigenvalue  $\alpha$  along the top  $A_3$  line in figure 6. This is the line which runs from the upper box edge to the righthand box edge. Along the profile we have marked the location and identity of the various singularity points along the  $A_3$  line.

lines trace the formation of multistream regions through time, forming the blueprint for the structure of the cosmic web.

The  $A_3$  lines delineate the points where the eigenvalues  $\alpha$  and  $\beta$  are maximal along the direction of the corresponding local eigenvector. At these points the gradient of the eigenvalue  $\lambda$  along the eigenvector direction is zero, i.e. they are the points where the eigenvector  $\mathbf{n}^\lambda$  is orthogonal to the eigenvalue gradient vector  $\nabla_q \lambda(\mathbf{q})$  (see fig. 5),

$$\mathbf{n}^\lambda \cdot \nabla_q \lambda = 0. \quad (18)$$

Relating this to the eigenvalue isocontours, we observe that these are the points where the deformation tensor eigenvector  $\mathbf{n}^\lambda$  is running tangential to the contour lines of the corresponding eigenvalue  $\lambda$ . In other words, the  $A_3^\lambda$  points on a  $A_2^\lambda$  line are those points where the eigenvector  $\mathbf{n}^\lambda$  is tangential to the contour  $A_2^\lambda$ . Moreover, as the extrema of  $\lambda(\mathbf{q})$  are defined by the condition  $\nabla_q \lambda = 0$ , they are always located on  $A_3^\lambda$  lines.

The physical significance of the  $A_3$  ridge defined by equation 18 may be understood when looking at the way in which a mass element on the line develops a singularity. To this end, we need to take along that the deformation of mass elements occurs along the eigenvector direction  $\mathbf{n}^\lambda$ . Because of the eigenvalue gradient's zero value in that same direction, there is a line-up and accumulation of neighbouring mass elements which simultaneously pass through the singularity. When mapped to Eulerian space, this evokes the formation of an  $A_3$  cusp. They are located at the tip of the evolving  $A_2$  fold singularity, which represent the Eulerian manifestation of the corresponding  $\lambda$  eigenvalue isocontour (see fig. 6 and fig. 5).

Hence, following this observation, we see that the  $A_3$  lines trace the location of the progenitors of  $A_3$  cusp singularities. Dependent on whether it concerns the lines for the first,  $\alpha$ , eigenvalue or the second,  $\beta$ , eigenvalue, we distinguish between the  $A_3^\alpha$  lines and the  $A_3^\beta$  lines. In fig. 5 we have indicated the  $A_3$  lines by means of heavy solid lines, where we have made a distinction between the  $A_3^\alpha$  lines (red) and the  $A_3^\beta$  lines. Note that the defining equation 18 generates a set of lines  $A_3^\lambda(\mathbf{q})$  that identify all points  $A_3^\lambda$ , regardless of the time when they become singular.

While the solution of equation 18 defines the  $A_3$  lines in Lagrangian space, for their full outline we also need to consider the points where they terminate. Interestingly, while the  $A_3$  lines are continuous smooth lines marking the location of progenitors of cusps, the lines terminate at isolated points.

One class of termination points relates to the trivial condition that the formal solution of equation 18 should not involve negative eigenvalues  $\lambda$ . These are excluded from consideration because they correspond to an expansion along the corresponding eigen direction, and will not be able to form a caustic. As a result, the  $A_3$  lines are truncated at the level set  $\lambda(\mathbf{q}) = 0$ . In reality, the  $\lambda = 0$  level set would never be reached: it would require an in-

finite time to reach the singularity. For this reason, in all our figures we fade the  $A_3$  lines as  $\lambda$  nears zero. Note that this condition occurs more frequently for the  $A_3^\beta$  lines: because  $\beta < \alpha$ , it has a negative value of a larger swath of Lagrangian space. A nice example of this can be seen in figure 6, in which the blue fading line indicates the location of the  $A_3^\beta$  line in the same area as the progenitor of an  $\alpha$ -caustic.

An even more profound and fundamental termination point of  $A_3$ -lines occurs in more subtle circumstances. While rare, there are points  $\mathbf{q}$  where both eigenvalues have the same value,  $\alpha(\mathbf{q}) = \beta(\mathbf{q})$ . At these points the eigenvectors have no preferred direction, rendering equation 18 meaningless. In subsection 4.6, we will elaborate on this class of points and demonstrate that they concern an isolated and discrete set of special points. They generate another class of caustics, the umbilics  $D_4$  (of which there are two types). Here, it is important to note that they do not form crossing points of  $A_3^\alpha$  and  $A_3^\beta$  lines, but rather their connecting tips. Figure 5 marks the location of the  $D_4$  singularities by means of a triangle.

Ideally, one would like to show the lines in a three-dimensional diagram, with the added dimension being time or, equivalently, the eigenvalue level  $\alpha$ . We would find that no  $A_3$  line intersects another  $A_3$  line: no Lagrangian point would ever pass at any one time through more than one singularity. Note that in fig. 5 we only show the Lagrangian plane. Even while the  $A_3$ -lines for the major and minor eigenvalues do seem to intersect at places, this has no physical meaning or implication.

#### 4.4 $A_3$ lines: the emergence & merging of pancakes

In figure 8, we have plotted the run of the eigenvalue  $\alpha$  along the large  $A_3^\alpha$  line (blue) running from top left to bottom right in figure 5. We can clearly distinguish the maxima of  $\alpha$  along this ridge. These points are marked as  $A_3^+$  and they are the Lagrangian progenitors of the first cusps emerging in the cosmic density field. The landscape of  $\alpha$  isocontours around one of these  $A_3^+$  points is illustrated in the lefthand panel of figure 3.

Once the cusp at the maximum  $A_3^+$  has emerged, the value of  $\alpha$  at which a point reaches singularity decreases as time proceeds,  $\alpha(\mathbf{q}) = 1/D(t)$ . At time  $t$ , all points on the corresponding  $\alpha$  isocontour become singular. These points pass through an  $A_2$  fold singularity and in Eulerian space become visible as  $\alpha$ -caustics that enclose a pancake. Two points stand out, the ones at the intersection of the  $A_3$  line and the  $\alpha$  isocontour. They are the ones that in Eulerian space will be visible as  $A_3$  cusps (fig. 6, righthand frame).

A particular example of a pancake forming around a maximum  $A_3^+$  is shown in figure 6. It shows a simple example of an  $A_3^+$  point and its immediate Lagrangian surroundings (lefthand panel), and the corresponding  $\alpha$ -caustic (pancake) in Eulerian space (righthand panel): the isocontours in the lefthand panel are the progenitors of

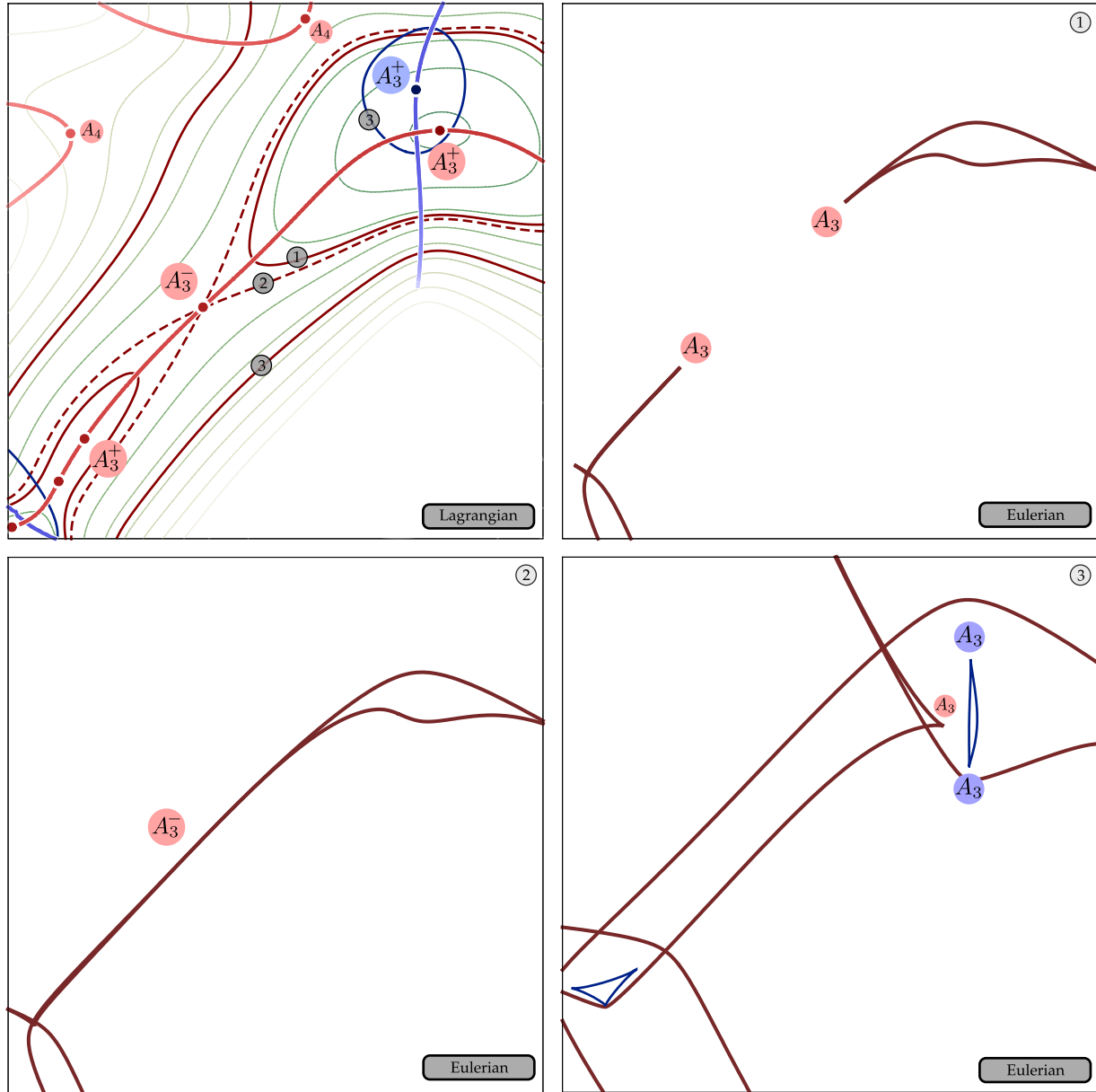


**Figure 9.** The merger of two pancakes. Top-left panel: Lagrangian space. Other panels show the evolution of caustics in Eulerian space. The progenitors of caustics in Lagrangian space are marked in correspondence with the stages shown in Eulerian space. Eulerian panel '2' shows exactly the instant of annihilation of two cusps at  $A_3^-$  point. Notations are similar to figure 6.

the caustic in the righthand panel. The Eulerian image is one of an expanding and growing pancake, enclosed by its  $\alpha$ -caustic and with two  $A_3$  cusp singularities at its tips. In its Lagrangian setting, we may appreciate how the corresponding singularity state - the progenitor of the caustic - gradually descends from the hill around  $A_3^+$ . The  $A_3$  cusps are clearly special of the caustic progenitor: they are the points on the Lagrangian progenitor's outline that traverse along the  $A_3$  line in an opposite direction.

An essential process for the development of the cos-

mic web is that of linking different structural elements into a connecting network. One important representative of this is the linking up between two growing pancakes. With pancakes emerging around the maxima  $A_3^+$  on  $A_3$  lines, their subsequent merging is intimately related to saddle points in the  $\alpha$  eigenvalue field. These saddles are the local minima  $A_3^-$  along the  $A_3$  lines (see fig. 8). Two pancakes that grow from two maxima  $A_3^+$  on the same  $A_3$  line, may merge when their cusps meet and annihilate

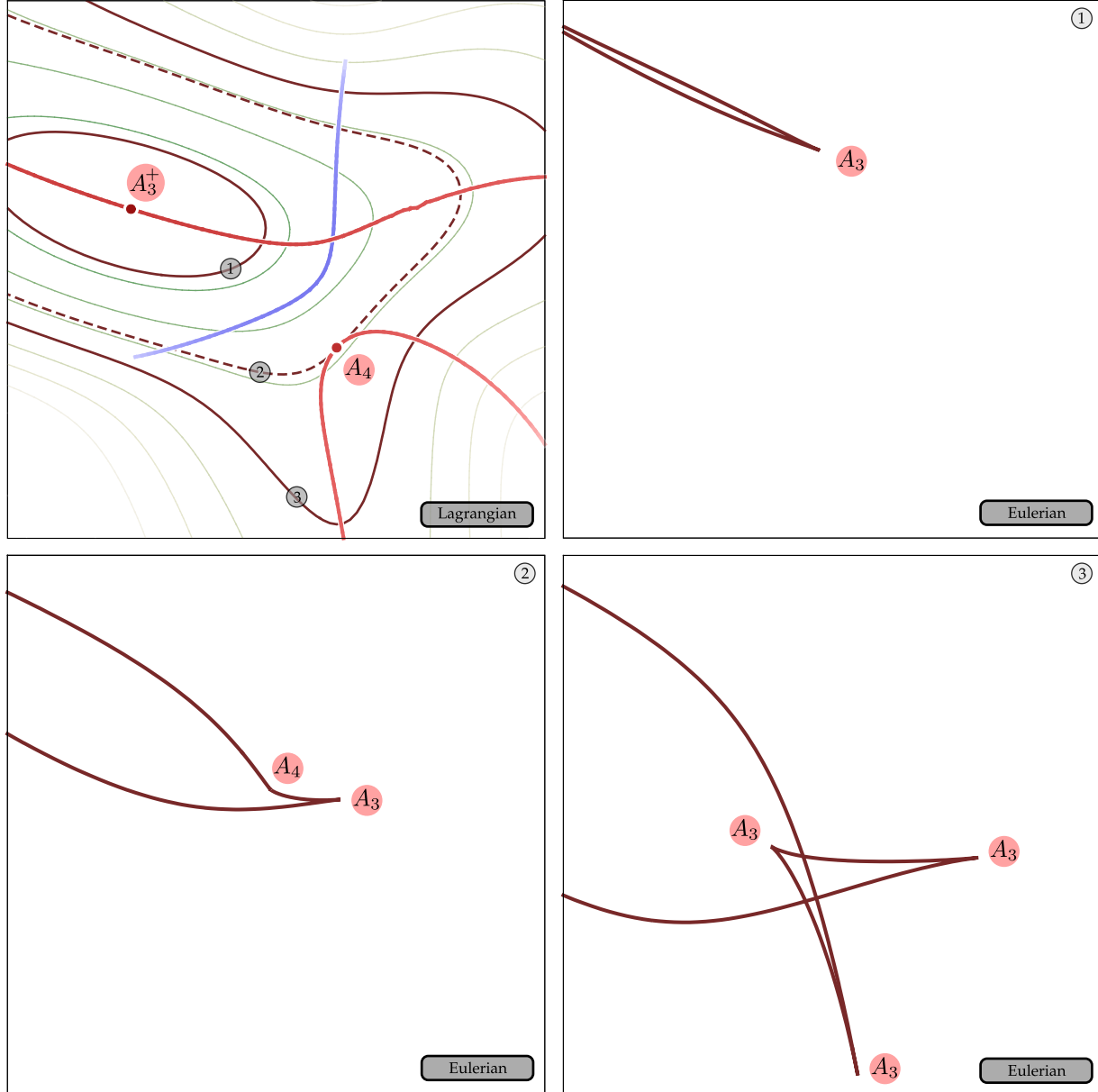


**Figure 10.** Formation of an  $A_4$  swallow-tail singularity. Top-left panel: Lagrangian view of the formation of an  $A_4$  singularity. The thick contours descend down  $\alpha$  as time increases. The dotted contour shows the moment at which the ‘swallow tail’ is formed. The three time steps indicated by these contours are shown in Eulerian space in sub figures 1, 2 and 3. The lines in those figures show the location of the caustics, by mapping the contours in the Lagrangian image to their Eulerian position.

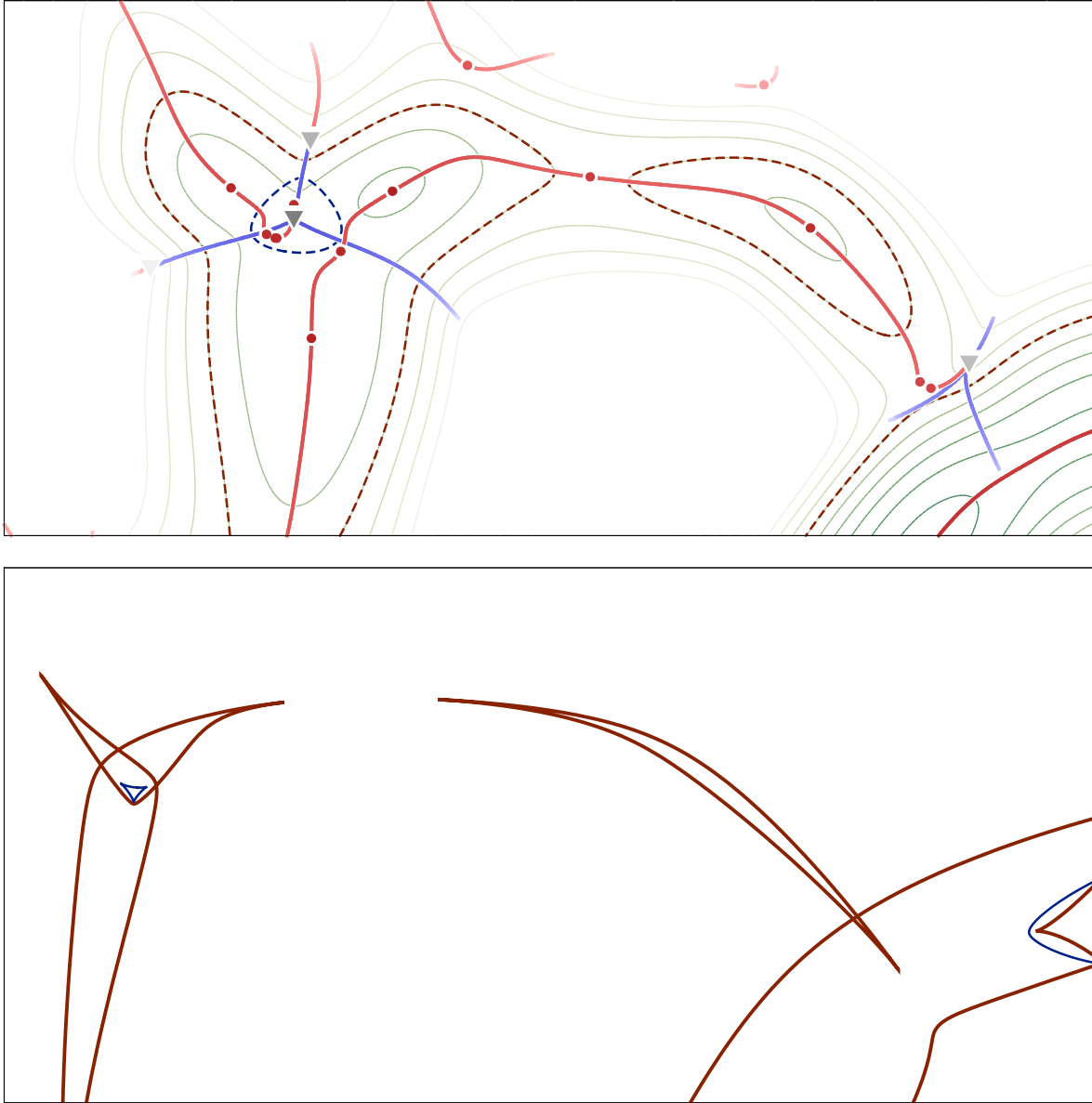
at the saddle point,  $A_3^-$  (see fig. 3 for the corresponding normal form illustration).

Figure 9 shows the merger of two pancakes. The top left panel shows the eigenvalue landscape in Lagrangian space. The remaining three panels illustrate the dynamics of the merging process, with the panel sequence marked from (1) to (3) in the right corner of each panel. In the Lagrangian panel we have marked three caustic progenitors, two  $\alpha$  caustics (red contours) and one  $\beta$  caustic (blue contours). In the corresponding Eulerian panels, we

have indicated them at the times they become caustics. In panel(1), we see the formation of two pancakes, each with a characteristic  $A_3$  cusp at their tip. In panel (2), we see the merging of the two pancakes into one structure and the annihilation of the two cusps. The merger location is the Eulerian location of the  $A_3^-$  saddle, whose Lagrangian position in the  $\alpha$  landscape between the two hills around the  $A_3^+$  points is clearly visible in the topleft panel.

The structure evolving in figure 9 also reveals the formation of a  $\beta$ -caustic. Its progenitor in the Lagrangian





**Figure 11.** Connection of caustic features and network formation. Top panel: deformation field, singularity location and  $A_3$  lines around a Lagrangian region with three disjoint caustic progenitors. Bottom: corresponding Eulerian region, in which the caustics have emerged. The caustic in the form of a simple pancake crosses the bottom caustic due to mapping. Further details are described in the text, sect. 4.5.

map is the hill around the  $A_3^+$  maximum of the  $\beta$  eigenvalue landscape, indicated by means of blue solid contours. The related  $A_3^\beta$  line is also visible in the same panel, as the blue solid line running approximately orthogonal to the (red)  $A_3^\alpha$  line. In the final (bottom righthand) panel, the corresponding  $\beta$  pancake is seen to emerge in Eulerian space. It is marked by the two  $A_3$  cusps at its tip.

An additional feature visible is the curvilinear triangle visible in the bottom lefthand corner of panel (3). It

is the result of a  $D_4$  metamorphosis. It will be discussed later, in section 4.6.

#### 4.5 $A_4$ points & swallow-tail singularities

The  $A_4$  singularity completes the list of generic singularities of the A-series occurring in two-dimensional potential type maps. The  $A_4$  singularities are also known as swallow tail singularities (for the corresponding normal form illustration, see fig. 3).

$A_4$  singularities are defined as the points where the eigen vector  $\mathbf{n}^\lambda$  is tangent to the  $A_3$  lines. A specific example of an  $A_4$  point in its Lagrangian environment can be seen in the top left panel of figure 10.  $A_4$  singularities are special in that they are the locations in the eigenvalue field  $\lambda$  at which three particular related vectors are colinear. These are the (i) the local eigenvector  $\mathbf{n}^\lambda$ , (ii) the local tangent to the  $A_2$  contour and (iii) the local tangent to the  $A_3$  line. From the definition in equation 18, regarding  $A-3$  lines we know that by definition the eigenvector is always tangent to the  $A_2^\lambda$  contour.

The fact that at  $A_4$  the eigenvector  $\mathbf{n}^\lambda$  is tangential to both the  $A_2$  and  $A_3$  line implies that the magnitude of the eigenvalue - along the  $A_3$  line on which the  $A_4$  point is located - reaches a local maximum. This may be directly appreciated from the example in figure 10. The Lagrangian map shows that the  $A_4$  singularity marks the location where the lower righthand  $A_3$  line reaches its highest point on the slope of the hill surrounding maximum  $A_3$ . The dashed isocontour marks the points where the eigenvalue  $\lambda$  has the same value as at  $A_4$ . Along the lower righthand  $A_3$  line, in both directions from  $A_4$ , the value of  $\lambda$  is lower than at  $A_4$ . Physically, at the points along the tangent  $A_3$  line we see a confluence of mass elements that almost simultaneously pass the  $A_3$  cusp singularity. This catastrophe leads to the emergence of a special kind of singularity, more complex than that of the  $A_3$  cusp, the  $A_4$  swallow tail.

An important observation is that the  $A_4$  singularity is a metamorphosis. The singularity exists only at one single moment of time, the moment  $t$  at which the value of  $\lambda$  at  $A_4$  is equal to  $\lambda = 1/D(t)$ . At this instant the  $A_2^\lambda$  line, whose identity is continuously evolving, touches the  $A_3$  line at  $A_4$ . In the situation of fig. 10 (top lefthand panel), at the moment of the  $A_4$  metamorphosis is the dashed isocontour the  $A_2$  line.

The significance of the  $A_4$  metamorphosis within the context of structure formation can be best understood by following the development of a representative example in Eulerian space. The three Eulerian panels (1) to (3) in figure 10 show three stages around the instant of  $A_4$  metamorphosis. In panel (1) we see the pancake that has formed around the maximum  $A_3^+$ . At this instant, isocontour (1) in Lagrangian space is the  $A_2$  line, which in Eulerian space maps into the *fold* caustic of the pancake. At the next timestep, we observe the sudden appearance of a *swallow tail*  $A_4$  singularity at the tip of the pancake (panel 2). This instant of  $A_4$  metamorphosis is the moment at which the Lagrangian dashed eigenvalue isocontour (2) has become the  $A_2$  line and touches singularity point  $A_4$ .

Following this instant of metamorphosis, the swallow tail disappears again and morphs into the complex four-edged configuration visible in panel (3). At the tip of the pancake, we find a two-wing protrusion defined by three  $A_3$  singularities. To understand this configuration, we should observe that there are three intersections of  $A_3$  lines with the  $A_2$  line, i.e. isocontour (3). There is one

such intersection with the upper  $A_3$  line and two with the lower righthand one. These three are the progenitors of the three  $A_3$  cusp singularities that we see in Eulerian panel (3). The other points on the  $A_2$  isocontour (3) map into the characteristic connecting caustic outline of panel (3). The first part of the Lagrangian isocontour (3), running from the leftside box boundary to the  $A_3$  point near the lower box boundary, maps into the Eulerian caustic's top edge and ends at the lower  $A_3$  cusp. The caustic's lower edge is the result of the mapping of the top section of the Lagrangian  $A_2$  line. The  $A_3$  point at the intersection of isocontour (3) with the upper  $A_3$  line is the progenitor of the  $A_3$  cusp at the tip of this caustic's branch. The two winglike caustic edges connecting to the third  $A_3$  cusp are stemming from the two righthand sections of Lagrangian contour (3), interspersed by the  $A_3$  point which is the progenitor of the connecting cusp.

The above example illustrates the instrumental role of  $A_4$  swallow-tail singularities in establishing the global connections between different sections of the cosmic web. The  $A_4$  singularities are the junction points at which disjoint pieces of Lagrangian  $A_3$  lines get connected. Observing this on a somewhat larger scale underlines the significance of this role. Figure 11 depicts a Lagrangian region (top panel) and its Eulerian equivalent at the instant at which the dashed contours have become  $A_2$  lines (bottom panel). At this moment, we may identify three independent sections of the cosmic web. The large lefthand structure has already passed the stage of  $A_4$  metamorphosis. It has resulted in the formation of a typical winglike configuration, established by the  $A_4$  singularity which in the Lagrangian map is located near the inner  $A_2^\beta$  line. The second, central, structure is a typical pancake. It is about to merge with the neighbouring complex once the  $A_2$  lines reach the  $A_3^-$  saddle point positioned along the connecting  $A_3$  line. The second  $A_4$  singularity, close to the  $A_2$  line at the edge of the lower righthand island, is on the verge of its metamorphosis. Once it materializes, it will produce two cusps that merge with the cusp that is already inside the lower righthand pancake visible in the Eulerian map.

#### 4.6 $D_4$ points: purses & pyramids

The final class of singularities to investigate in their field setting are the  $D_4$  singularities. These belong to a different family than the  $A$ -type singularities that we have discussed in the previous subsections.

The principal difference between the two families of singularities, the  $A$ - and  $D$ -type singularities, is that of the number of eigenvalues on which they depend. Singularities in the  $A$ -family depend on only one eigenvalue,  $\alpha$  or  $\beta$ .  $D$ -type singularities, on the other hand, involve both eigenvalues  $\alpha$  and  $\beta$ .

$D_4$  singularities are the points at which both eigenvalues have the same value,  $\alpha = \beta$ . In Lagrangian space, the singularities occur at isolated points. At first, this might occur as counterintuitive. In 2-dimensional space,





**Figure 12.**  $D_4$  singularities and  $A_3$  line connections. The figure shows the location of three  $D_4$  singularities in Lagrangian space. The  $D_4$  locations are indicated by a red dot inside a red circle. The black lines are  $A_3^\alpha$  lines, while the grey lines are  $A_3^\beta$  lines. The panel contains two *purse* singularities ( $D_4^+$ ) and one *pyramid* singularity ( $D_4^-$ ).

one would expect the solution of an equation

$$\alpha(\mathbf{q}) = \beta(\mathbf{q}) \quad (19)$$

to define a continuous line. However, upon closer inspection one may realize that - at any particular instant  $t$  - equation 19 is equivalent to two independent equations, yielding a single point as solution. Within this context, it is good to realize that we are dealing with a highly constrained situation, in which the two eigenvalues  $\alpha$  and  $\beta$  are strongly correlated and are conditioned by the requirement that  $\alpha \geq \beta$ .

#### 4.6.1 The $D_4$ equation

Given the deformation tensor  $d_{ik} = -\partial s_i / \partial q_k$ , its eigenvalues  $\lambda$  are the solution to the secular equation,

$$\begin{pmatrix} d_{11} - \lambda & d_{12} \\ d_{12} & d_{22} - \lambda \end{pmatrix} = 0. \quad (20)$$

This translates into the corresponding secular quadratic equation,

$$\lambda^2 - (d_{11} + d_{22})\lambda + d_{11}d_{22} - d_{12}^2 = 0, \quad (21)$$

whose two solutions are given by

$$\lambda_{1,2} = \frac{1}{2} \left( d_{11} + d_{22} \pm \sqrt{(d_{11} - d_{22})^2 + 4d_{12}^2} \right). \quad (22)$$

In order to have  $\alpha = \beta$ , two independent conditions need to be satisfied simultaneously,

$$\begin{aligned} d_{11}(\mathbf{q}) &= d_{22}(\mathbf{q}), \\ d_{12}(\mathbf{q}) &= 0. \end{aligned} \quad (23)$$

Each of these two equations describes a line. Their combined solution consists of the discrete points  $\mathbf{q}$  at the intersection of these lines. The  $D_4$  singularities are therefore

located at a set of isolated points (see appendix B). Notice that the identity of these isolated points is changing as a function of time. Throughout this study, we have used reverse triangles to indicate the location of the  $D_4$  singularities in the various figures (e.g. fig. 5).

Because of the equality of the two eigenvalues, the eigenvectors at  $D_4$  are degenerate: any arbitrary 2-D vector may function as eigenvector. It is yet another manifestation of the non-Gaussian nature of the eigenvalue  $\lambda$  fields.

#### 4.6.2 the $D_4$ location: $A_3$ lines.

The role of  $D_4$  singularities in outlining the cosmic web becomes clear when evaluating their location in the Lagrangian eigenvalue field. They have a special position on the  $A_3^\alpha$  and  $A_3^\beta$  lines. While located on both lines, they are not found at the crossing of two such lines. Instead, they are connection points between two such lines, located at the tip of an  $A_3^\alpha$  line and a connecting  $A_3^\beta$  line.

The first aspect of importance is the fact that also  $D_4$  points are located on  $A_3$  lines. This may be directly understood from the degeneracy of the corresponding eigenvectors. Without loss of generality, the eigenvector  $\mathbf{n}^\lambda$  at  $D_4$  points can always be oriented such that it is orthogonal to the gradient of the field. It therefore fulfils the  $A_3$  condition,  $\mathbf{n}^\lambda \cdot \nabla_q \lambda = 0$  (eqn. 18). Because this is true for both eigenvalues  $\alpha$  and  $\beta$ , any  $D_4$  point is located on  $A_3^\alpha$  and  $A_3^\beta$  lines.

It may be instructive to look at the formal derivation of the above. To this end, we evaluate the inner product  $I_\lambda(\mathbf{q})$  of the normal vector  $\mathbf{n}(\mathbf{q})$  and the gradient of the eigenvalue field,

$$\begin{aligned} I_\lambda(\mathbf{q}) = \mathbf{n}^\lambda \cdot \nabla_q \lambda &= \begin{pmatrix} n_1 \\ n_2 \end{pmatrix} \cdot \begin{pmatrix} \partial\alpha/\partial q_1 \\ \partial\alpha/\partial q_2 \end{pmatrix} \\ &= n_1 \frac{\partial\alpha}{\partial q_1} + n_2 \frac{\partial\alpha}{\partial q_2} \end{aligned} \quad (24)$$

To calculate  $I_\lambda(\mathbf{q})$ , we recast its expression in terms of the deformation tensor  $d_{ij}$  and its derivatives

$$t_{ijk} \equiv \frac{\partial d_{ij}}{\partial q_k}, \quad (25)$$

and the eigenvector  $\mathbf{n}^\alpha$ , whose components are given by

$$\mathbf{n}^\alpha = \begin{pmatrix} d_{12} \\ \alpha - d_{11} \end{pmatrix}. \quad (26)$$

The tensor  $t_{ijk}$  has only four independent components:  $t_{111}, t_{112}, t_{122}$  and  $t_{222}$ . The other components  $t_{ijk}$  can be inferred from these on the basis of symmetry considerations.

Differentiation of the secular equation 21, for eigenvalue  $\lambda = \alpha$ , yields an expression for the components of

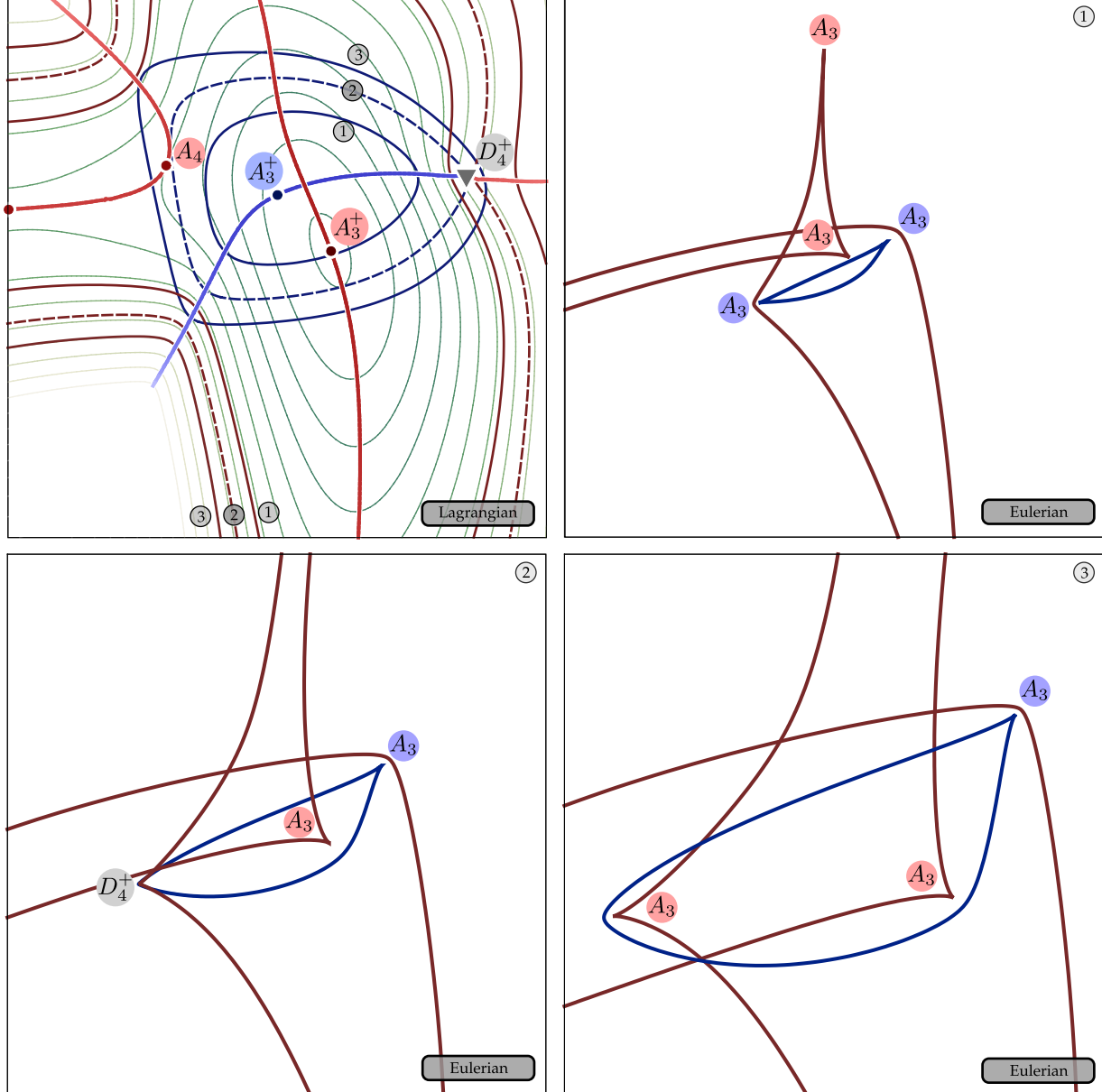


**Figure 13.** The purse. The setup of this figure is the same as in figure10. The three sets of contours in the top left image are shown in Eulerian view in the other three subfigures. We start at an evolved stage, the red contour has already passed the  $A_3^+$  and  $A_4$  points, so the separate  $A_3$  lines are now a single structure. The second eigenvalue (blue) has formed a pancake inside this structure. This type of conjunction is often encountered. As the contour of the second eigenvalue is moving out it passes the  $D_4^+$  point. Note that in the Eulerian view this event is mirrored, it happens on the left-most cusp, due to the change of parity inside the three-stream region. The cusp changes its colour to red. The second blue cusp is also nearing the red caustic, but as the corresponding  $D_4^+$  point lies in a region where both eigenvalues are negative, they will never join.

the gradient vector  $\nabla_q \alpha$ ,

$$\begin{aligned} (2\alpha - d_{11} - d_{22}) \frac{\partial \alpha}{\partial q_i} - \alpha(t_{11i} + t_{22i}) \\ + (d_{22}t_{11i} + d_{11}t_{22i}) - 2d_{12}t_{12i} = 0. \end{aligned} \quad (27)$$

Multiplication of these expressions for the gradient components by the corresponding components of the eigen-

vector  $\mathbf{n}^\alpha$  (see eqn. 26) leads to the following expression for the inproduct,

$$\begin{aligned} I_\alpha(\mathbf{q}) &= d_{12}[(\alpha - d_{22})t_{111} + (\alpha - d_{11})t_{122} + 2d_{12}t_{112}] \\ &+ (\alpha - d_{11})[(\alpha - d_{22})t_{112} \\ &+ (\alpha - d_{11})t_{222} + 2d_{12}t_{122}]. \end{aligned} \quad (28)$$

To obtain this expression, we have used the fact that the

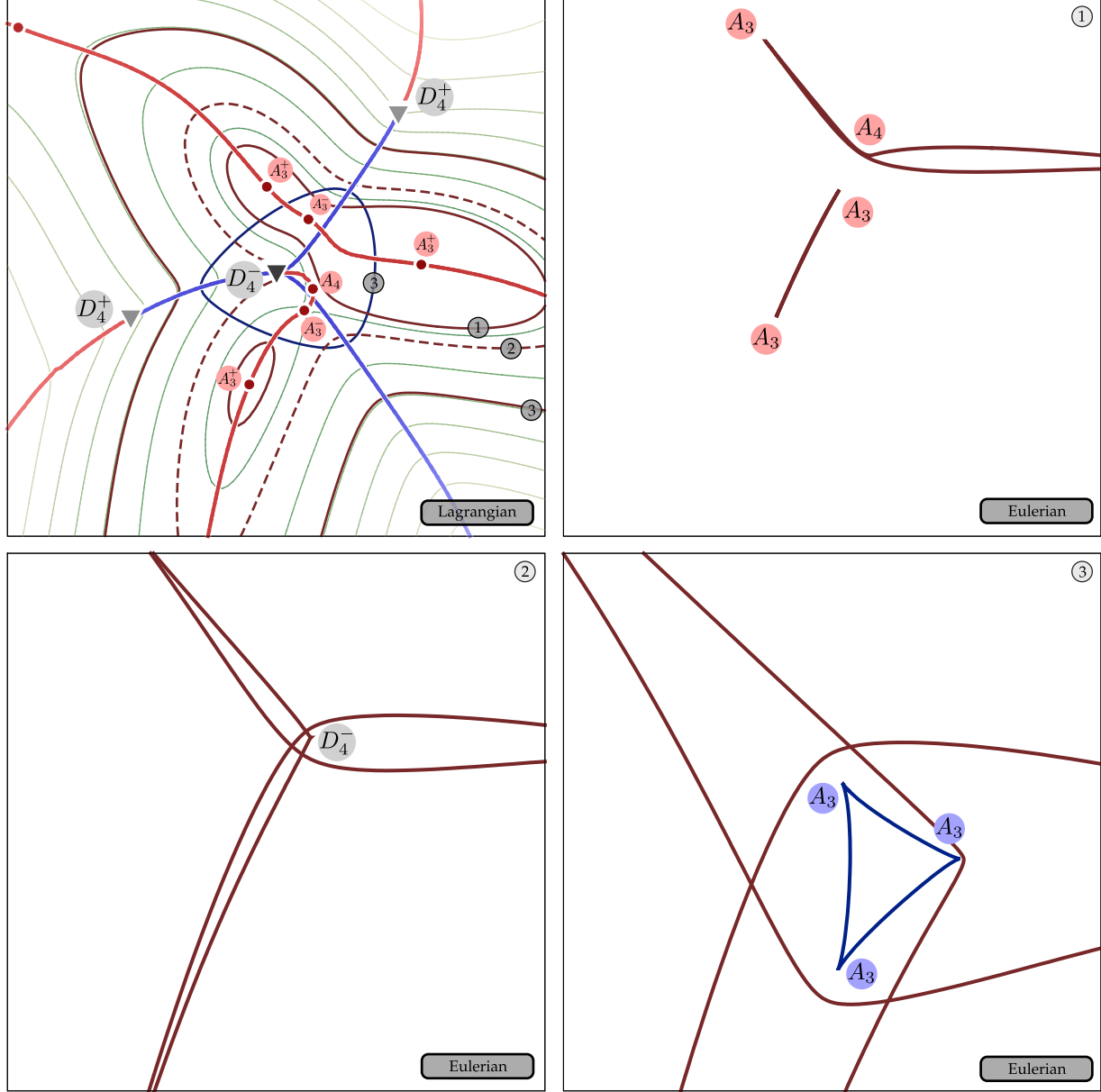


**Figure 14.** The pyramid. We return to the setting illustrated in figure 5. Almost all singularities that we know of in 2D are represented in this figure. In the first image we see two pancakes, one of which is close to getting a swallow-tail. The resulting cusp merges soon at the bottom most  $A_3^-$  point, while the other end heads for the pyramid  $D_4^-$ . The  $D_4^-$  is approached from three sides, but those are in a very tiny loop that we don't resolve in this image. The resulting three  $\beta$ -cusps expand outwards. Two of them will turn to  $\alpha$ -cusps at the purses  $D_4^+$ .

trace of the deformation tensor is equal to the sum of the eigenvalues, so that

$$\begin{aligned} 2\alpha - d_{11} - d_{22} &= \alpha - \beta, \\ 2\beta - d_{11} - d_{22} &= \beta - \alpha. \end{aligned} \quad (29)$$

By means of some algebraic manipulation, we may rewrite

the expression for  $I_\alpha(\mathbf{q})$  into a more convenient form,

$$\begin{aligned} I_\alpha(\mathbf{q}) &= (\alpha - d_{22}) [d_{12}t_{111} - (\alpha - d_{11})t_{112}] \\ &+ (\alpha - d_{11}) [d_{12}t_{122} - (\alpha - d_{11})t_{222}] \\ &+ 2d_{12} [d_{12}t_{112} - (\alpha - d_{11})t_{122}]. \end{aligned} \quad (30)$$

Given that  $I_\alpha(\mathbf{q})$  is a scalar quantity, we may evaluate it in the eigenvector coordinate system, for which  $d_{11} = \alpha$ ,  $d_{22} = \beta$  and  $d_{12} = 0$ . The situation in which both eigenvalues are equal,  $\alpha = \beta$ , then leads to the conclusion

that

$$I_\alpha(\mathbf{q}) = 0. \quad (31)$$

In other words, given that the condition that  $\alpha = \beta$  implies that  $I_\alpha(\mathbf{q}) = 0$  and thus fulfils the  $A_3$  line condition stated in equation 18, we are lead to the conclusion that the  $D_4$  points are located on  $A_3$  lines.

#### 4.6.3 The $D_4$ location: $A_3$ termination points

Given that  $D_4$  points belong to both  $A_3^\alpha$  and  $A_3^\beta$  lines, one might at first expect them to mark the crossing point between these lines. However, this turns out not to be the case. Instead, they mark the connection points of  $A_3^\alpha$  and  $A_3^\beta$  lines, both terminating at that specific  $D_4$  point. Thus,  $D_4$  are points where  $A_3^\alpha$  and  $A_3^\beta$  lines meet.

We may understand this by considering the three-dimensional space  $(q_1, q_2, \lambda)$  defined by the Lagrangian plane and the eigenvalue  $\lambda$ . This would be the altitude map shown in maps like that of figure 5. When looking at the 2-D map in the Lagrangian plane  $(q_1, q_2)$ , the  $A_3^\alpha$  and  $A_3^\beta$  lines may appear to intersect. However, this is merely an artefact of the projection of both lines on to the  $(q_1, q_2)$  space. In reality, they cannot intersect because in general  $\alpha \geq \beta$ : when a given Lagrangian position  $(q_1, q_2)$  is located on both an  $A_3^{\alpha\text{pha}}$  line and a  $A_3^\beta$  line, at that location the  $A_3^\alpha$  line will lie at a higher altitude in the 3D  $(q_1, q_2, \lambda)$  space. The only exception is when  $\alpha = \beta$ , i.e. at the  $D_4$  points.

The image is one where the  $A_3^\alpha$  line and  $A_3^\beta$  line meet smoothly at  $D_4$  points. One one side of a  $D_4$  point we find the  $A_3^\alpha$  line, on the other the  $A_3^\beta$  line.

#### 4.6.4 Purses and Pyramids

There are two classes of  $D_4$  points. One class is the *purse* singularity  $D_4^+$ . These points connect one  $A_3^\alpha$  with one  $A_3^\beta$  line. The structure of caustics and their progenitors in the vicinity of  $D_4^+$  singularity is shown in figure 13.

The second class is the *pyramid* singularity  $D_4^-$ . The  $D_4^-$  points form the connections of six lines  $A_3$ , three  $A_3^\alpha$  and three  $A_3^\beta$  lines. We may appreciate this in figure 5 and 14, which shows the caustics and their progenitors around a  $D_4^-$  singularity. Typically, in the  $D_4^-$  situation, two of three connecting  $A_3^\lambda$  lines are small loops. In figure 12, we find a small loop of  $A_3^\alpha$  lines (black) and an even smaller loop of  $A_3^\beta$  lines (grey). Quite often, these loops are so small that an image hardly manages to resolve them (see the  $D_4$  point in e.g. fig. 5 and fig 14, see appendix B).

The type of the  $D_4$  type is determined by the sign of the quantity  $s_D$ ,

$$s_D \equiv t_{111}^2 t_{222}^2 - 3t_{112}^2 t_{122}^2 - 6t_{111} t_{112} t_{122} t_{222} + 4t_{111} t_{122}^3 + 4t_{222} t_{112}^3. \quad (32)$$

If  $s_D$  is positive, the singularity is a  $D_4^+$  purse singularity. Otherwise, it is a  $D_4^-$  pyramid singularity (Rozhanskii & Shandarin 1984).

## 4.7 Metamorphoses & transient singularities

The inventory of singularities in section 3 and the inventory of their position within the cosmic deformation field in the previous subsections forms the basis for our understanding of the evolution of of structure in terms of that of the network of caustic structures.

As we may already have appreciated, the evolution proceeds via a series of *metamorphoses*. A metamorphosis – perestroika in Russian – is a transient singularity that may still be considered stable in the sense that a perturbation of the manifold will only change the time and location of the event: a metamorphosis cannot be removed by perturbation.

Each metamorphosis involving singularities from the  $A$ -series results in a change in the global topology of the network. The systematic inventory of the fundamental singularities in terms of their normal forms that we present below allows us to appreciate how a system of folds and cusps changes topology as it passes through the transient singularities of metamorphoses.

A nice illustration of the latter is that in terms of the only two stable types of singularities, stable in the sense that they persist in time. These are the *fold* ( $A_2$ ) and the *cuspl* ( $A_3$ ) singularity (see fig. 6). Their time evolution is straightforward, in that it only involves their movement. In section 4.4 we have seen that the combination of fold and cuspl singularities defines the formation of a pancake. Starting from its tenuous embryonic state, a pancake grows in length as the bounding cusps at its tip move apart and the pancake region, in between the two cusps and enclosed between two fold caustics, gradually thickens. This growth gradually slows down.

In the physical reality of a gravitational system, these transitions work to increase the complexity of the system. A direct manifestation of the process in which matter passes through the shocks of singularities is that matter passes into regions with a larger number of streams than before.

## 5 THE COSMIC WEB: ASSEMBLY & LAGRANGIAN BLUEPRINT

In the previous section 4, we have noticed the central role of  $A_3$  lines in outlining and defining the structure that emerges as a result of gravitational evolution.  $A_3$  lines form the Lagrangian blueprint of structures found in the Cosmic Web, and may be regarded as its spine.

In this section we investigate the connection between the  $A_3$  spine and the emerging Cosmic Web. As a step-up towards the systematic discussion, we first look at a case study of the structure evolving in a typical specimen of a key region in the cosmic web. Having established in the previous section the identity and role of the various  $A$ - and  $D$ -class singularities, it is instructive and helpful for our intuition to observe the time evolution of the caustic structure in a small and characteristic Lagrangian region.

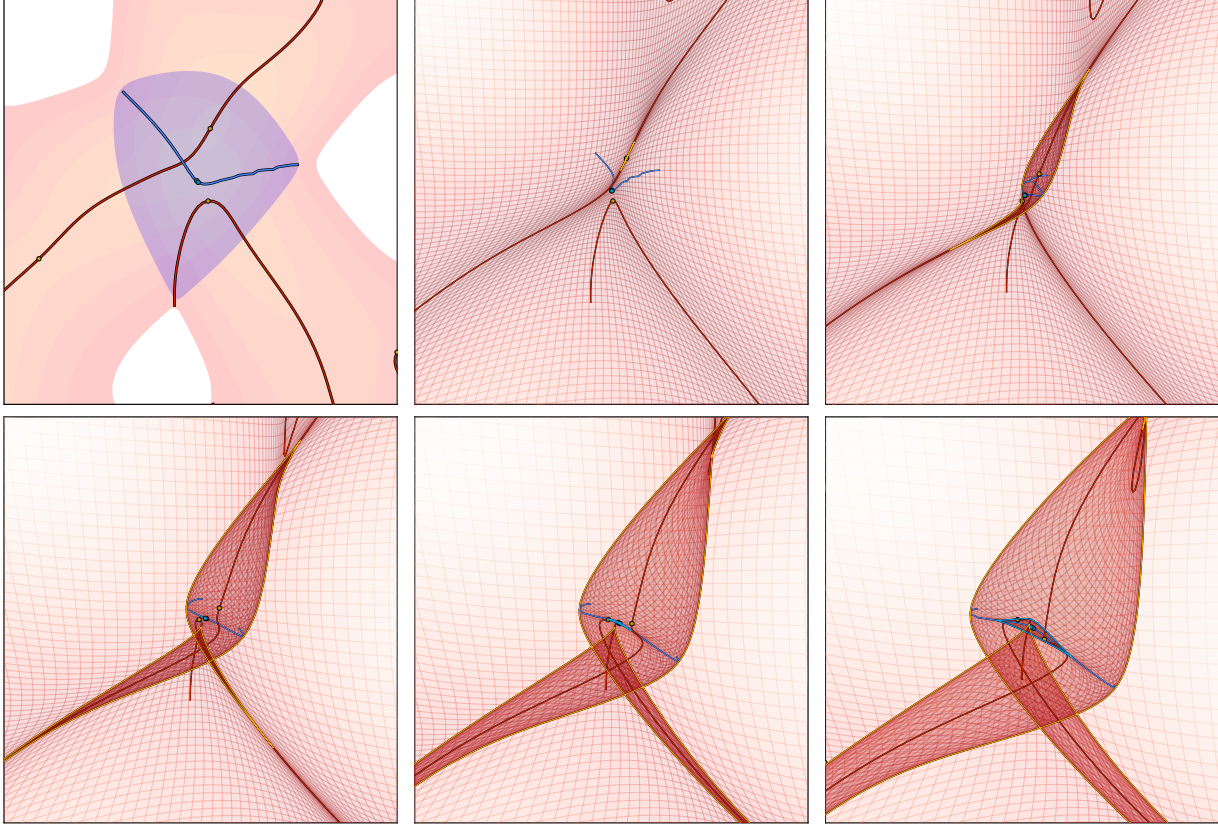


**Figure 15.** Evolving caustic structure around a cosmic web node. Time evolution of the Lagrangian region shown in the top left panel. Left top panel: Lagrangian space.  $A_3^\alpha$  lines – red,  $A_3^\beta$  line – blue. Light brown region shows  $\alpha > 0$ , blue is the region where  $\beta > 0$ . The top yellow dot shows a maximum of  $\alpha$ , the bottom yellow dot shows  $A_4$  and a dot on the left marks a saddle point. A blue dot shows a maximum of  $\beta$ . Middle top panel: Eulerian space at the time when  $\alpha$ -pancake just have emerged as a yellow thick line on the top yellow dot above the blue line. The remaining four panels show the region at different stages of caustic evolution, representing a highly common sequence of events.

### 5.1 Caustic Synergy: assembly of structure around a node

Figure 15 shows five stages during the evolution of the caustic structure around a small Lagrangian region, shown in the top lefthand panel. Following the Lagrangian panel is a sequence of five panels showing the evolving structure in the corresponding region in Eulerian space. The sequence runs from a very early epoch, in the top central panel, to a highly advanced one in the bottom righthand panel.

The four-dimensional Lagrangian submanifolds that define the phase space density field get deformed in time as matter elements flow pursue their path  $(\mathbf{q}, \mathbf{x})$ . The Eulerian position  $\mathbf{x}$  of each mass element is dependent on time, while the projection of their position in Lagrangian space,  $\mathbf{q}$ , remains fixed. The projection of the progenitors of caustics and  $A_3$  lines on to the Lagrangian plane is shown in the top lefthand panel of figure 15, while the changing projection to the Eulerian plane is the subject of the additional five panels.

The projection to Lagrangian space is nonsingular

and geometrically simpler and more transparent. Moreover, knowledge of the Lagrangian projection helps substantially in understanding and making sense of the Eulerian projection.

#### 5.1.1 The Lagrangian Spine

In the Lagrangian panel, the light brown shaded region demarcates the regions of positive deformation tensor eigenvalue  $\alpha$ . The light blue shaded region has a positive eigenvalue  $\beta$ .

Three  $A_3$  lines form the spine of the emerging web in this region. The two red lines are  $A_3^\alpha$  type lines, the blue line a  $A_3^\beta$  line. On the upper  $A_3^\alpha$  line, the yellow dot indicates the position of an  $A_3^+$  maximum. Note that it is also located within the light blue region. Another dot is a  $A_3^-$  minimum along the  $A_3$  line, a saddle point in the eigenvalue  $\alpha$  field. A blue dot on the  $A_3^\beta$  line marks the location of the  $A_3^\beta$  maximum.

The lower  $A_\alpha$  line does not run throughout the entire region: it stops at the contour  $\alpha = 0$ . As has been

discussed in section 4.3, structure does not develop in regions with negative  $\alpha$ . Of high relevance for the emerging pattern in Eulerian space is that the dot at the tip of the lower  $A_3^\alpha$  line is an  $A_4^\alpha$  point.

The identity of the various lines and points in the Lagrangian region determine the nature of the emerging structure in Eulerian space. The five Eulerian panels show the evolving density field. In the maps, the density is represented by the colour intensity, running from white in the underdense regions to dark red in high density collapsed regions.

The black solid lines are the mapping of the Lagrangian  $A_3^\alpha$  lines to Eulerian space, while the blue solid line represents the corresponding mapping of the  $A_3^\beta$  line. It is very instructive to follow the displacement and gradual merging, morphing, stretching and twisting of the  $A_3$  lines as we see the development of the structure in the density field. It immediately reveals the essential nature of these lines in the formation of the geometric pattern: they clearly function as the - flexible - spine of the web.

### 5.1.2 The Eulerian Assembly

The earliest depicted timestep is that shown in the top central panel. At this stage, we observe the emergence of the first  $\alpha$  pancake. It forms at and immediately around the  $A_{3+}$  point on the upper  $A_3^\alpha$  line in the Lagrangian panel. At this early stage, the pancake is so thin that its two caustic edges lie indistinguishably on top of each other. The next stage is shown in the top righthand panel. The central pancake has grown in extent, and has attained its classical morphology in which its inner region is enclosed by two *fold* caustics, which are connected into a single closed contour by the two *cusps* at its tip. The interior region is a three-stream region. The panel shows the structure just before the emergence of the  $A_4^\alpha$  swallow-tail singularity.

Already just before the  $A_4^\alpha$  singularity, we can see that the two  $A_3^\alpha$  lines are on the verge of connecting into one structure around a characteristic three-edged backbone. At the next stage, shown in the bottom lefthand panel, we find the complex caustic structure that formed in the aftermath of the  $A_4^\alpha$  singularity. The characteristic swallow-tail pattern consisting of three protrusions is defined by four caustic edges connected by four cusps. Three cusps connect the four caustics at the lower end, while the fourth one closes the caustic outline at the top of the configuration (also compare the structure in the bottom righthand panel of figure 10). While most of the interior of the caustic configuration involves a three-stream region, the small internal zone enclosed by four caustics is a region with a five-stream flow field.

During the most advanced stages of development, shown in the bottom centre and righthand panel, we see the growth and expansion of the  $\alpha$ -caustic structure that we found in the third timestep. In addition, we find the emergence and formation of  $\beta$ -pancake, within the con-

finer of the large  $\alpha$  pancake and around the  $A_3^\beta$  maximum (blue dot, Lagrangian map).

The emergence of the  $\beta$  pancake goes along with the formation of another five-stream flow in its interior. At the last timestep, we find that even a seven-stream region has formed in a small part of the  $\beta$  pancake. It is the result of the intrusion of the inner  $A_3$  cusp into the interior of the  $\beta$  pancake. This leads to an intersection of the two five-stream regions, which produces a seven-stream region.

## 5.2 The role and significance of $A_3$ lines

All point-like singularities are located on  $A_3$  lines. The direct implication of this is that all dynamically significant processes and events take place in the vicinity of the  $A_3$  lines. Singularities in the evolving density field are associated with the maxima, saddle points and minima of the deformation tensor eigenvalues  $\lambda$ . In addition, also the special  $A_4$  and  $D_4$  points are located on  $A_3$  lines.

Each  $\alpha$ -pancake originates at a maximum of  $\alpha$ . The pancake is enclosed by two *fold* caustics, whose progenitors are  $A_2^\alpha$ -lines. Two cusps at the tips of the pancake connect the *fold* caustics into a closed pancake boundary. The progenitors of the cusps are  $A_3$  points which traverse the  $A_3$  line in opposite direction as the pancake grows in time. In Eulerian space, the pancake enclosed by two caustics is a three-stream region, where mass elements with from a different Lagrangian origin are crossing each other.

The saddle points corresponding  $A_3^-$  minima along an  $A_3$  line are the progenitors of the points at which the cusps of two pancakes meet and annihilate, leading to the merging of the two pancakes into one larger one.

## 5.3 Global geometry and topology of $A_3$ lines

The global geometry and topology of the caustic structure emerging as the density field evolves is to a large extent determined by the characteristics of the  $\alpha$ -field, i.e. of the spatial distribution of the first eigenvalue  $\alpha$  of the deformation field.

The previous section has taught us that in particular the  $A_3^\alpha$  lines are instrumental in setting the spatial outline of the cosmic web. The evolution of the cosmic web, and in particular that of the connectivity between its main elements, can be largely deduced from the run of the  $A_3$  lines and the distribution of singularity points along their edge. Mainly because collapse along the  $A_3^\beta$  lines is always happening - usually substantially - after that along the  $A_3^\alpha$  lines, their effect on the percolation and topology of the network is at most marginal.

In principle, an  $A_3$ -line runs from one  $D_4$  point to another. However, the corresponding eigenvalue may drop below zero. In reality, structure evolution will not proceed to this point as it would never reach it within a finite time. One might therefore limit the dynamical evolution to a maximum cosmic time. The limiting time would limit the range of values for the eigenvalues  $\alpha$  and  $\beta$ . For example,



one may limit the time over which the density field has evolved to a level at which the density perturbations have a  $\sigma_\delta(t^*) \sim 1$ . At this stage the ZA would still give a crude but qualitatively reasonable approximation to the true evolution of a gravitating medium (Coles, Melott & Shandarin 1993; Melott, Pellman & Shandarin 1994). If at this point of time the linear growth factor  $D(t^*) = D^*$ , the minimum eigenvalue up to which we can still follow the evolution would be  $\lambda^* = 1/D^*$ . For lower values of  $\lambda$  we would no longer trust the approximation.

The segments of  $A_3$ -lines that satisfy the condition that  $\alpha \geq \lambda^*$  form a set of disconnected lines in L. These segments correspond to values of the eigenvalue  $\alpha$  that will be reached within the time in which the Zel'dovich approximation remains a good description of the full gravitational evolution. The isolated  $A_3$  line segments often contain small loops and bifurcation points. However, in general they are not connected to other  $A_3$  line segments. By implication, the set of  $A_3$  segments will not be able to form a percolating network in Lagrangian space.

The situation is somewhat different when we turn towards the emerging structure in Eulerian space. When mapped from Lagrangian to Eulerian space, different structures that are disjunct in the Lagrangian context get connected. The  $A_4$  singularities are instrumental in settling these connections. We saw a nice illustration of this in figure 11. It shows a pancake which has been mapped into the interior of another pancake. The latter is on the verge of passing through an  $A_4$  singularity. This will establish a connection between the corresponding pancake and the small central one. In turn, the latter will merge by means of an  $A_3^-$  saddle point with the nearby swallow tail configuration, thereby establishing a pervasive connection between all structural features in the region.

#### 5.4 Density profiles

For a complete inventory of the cosmic mass distribution in and around the cosmic web, we not only need to understand the connectivity of the various components but also the density distribution. The density distribution in the vicinity of all singularities is always highly anisotropic. Nonetheless, we obtain an adequate first order description of the mass distribution around a singularity by evaluating its radially averaged density profile.

Analytical expressions for the radial density profile around singularities are known. In particular, this concerns the averaged profile  $\bar{\rho}(r)$  as a function of radius  $r$  (in Eulerian space),

$$\bar{\rho}(r) = \frac{3M(r)}{4\pi r^3}, \quad (33)$$

where  $M(r)$  is the mass contained within a distance  $r$  from the centre of the singularity.

All singularities have a power-law average density profile,

$$\bar{\rho}(r) \propto r^{-n}, \quad (34)$$

in which the power law index  $n$  is dependent on the identity of the singularity. Singularities  $A_2$ ,  $A_3$ ,  $A_4$ , and  $D_4$  have power law slopes  $n = 1/2$ ,  $2/3$ ,  $3/4$ , and 1 respectively (Vasiljev 1977).

The  $D_4$  class singularities, at which the two eigenvalues  $\alpha$  and  $\beta$  have the same value, have the steepest density profiles. Notwithstanding this observation, it is good to emphasize that the collapse at these points is highly anisotropic. This may be immediately inferred from figures 13 and 14.

#### 5.5 Relation to structure in N-body simulations

Having developed the formalism for the geometrically outlining the backbone of the cosmic web, and the identification of the defining singularities and their connections, for assessing its relevance with respect to the fully developed cosmic mass distribution we resort to a comparison with the outcome of N-body simulations.

The Zeldovich approximation successfully describes the first stages of the development of the nonlinear mass distribution. These are the stages at which we see the transition of the cosmic density field from its primordial Gaussian origins to the far more complex and rich structure that we observe in the present-day Universe. The cosmic web is the manifestation of structure evolution at that quasi-linear stage. The subsequent gravitational evolution of the cosmic mass distribution is far more complex, and involves the hierarchical buildup of structure resulting in a rich multiscale spatial pattern of voids, walls, filaments and clumps characterized by a large range of scales and densities.

Here, we show how  $A_3$  lines relate to the structure that developed in the equivalent two-dimensional N-body simulation. The initial conditions of the N-body simulation consist of the same Lagrangian density field used for the singularity analysis. The simulation was carried out with a standard PM N-body code. The mass resolution and force resolution are equal. The simulation consists of  $1024^2$  particles, and forces are computed on a uniform  $1024^3$  grid. The initial power spectrum is a power law spectrum,

$$P(k) \propto k^{-1}, \quad (35)$$

which is statistically equivalent to the three dimensional power law power spectrum  $P(k) \propto k^{-2}$ . The fluctuation field realization has been Gaussian smoothed on a scale of "ngrid" gridcells.

##### 5.5.1 Phase Space Sheet & Mass Cell Parity Flips

The identification of the progenitors of structures in Lagrangian space is based on a novel technique that has been developed within the context of the phase space sheet description of cosmic structure (Tremaine 1999; Shandarin 2011; Shandarin, Habib & Heitmann 2012; Abel et al. 2012; Falck et al. 2012; Neyrinck 2012; Shandarin & Hidding 2013). The phase space sheet description looks at

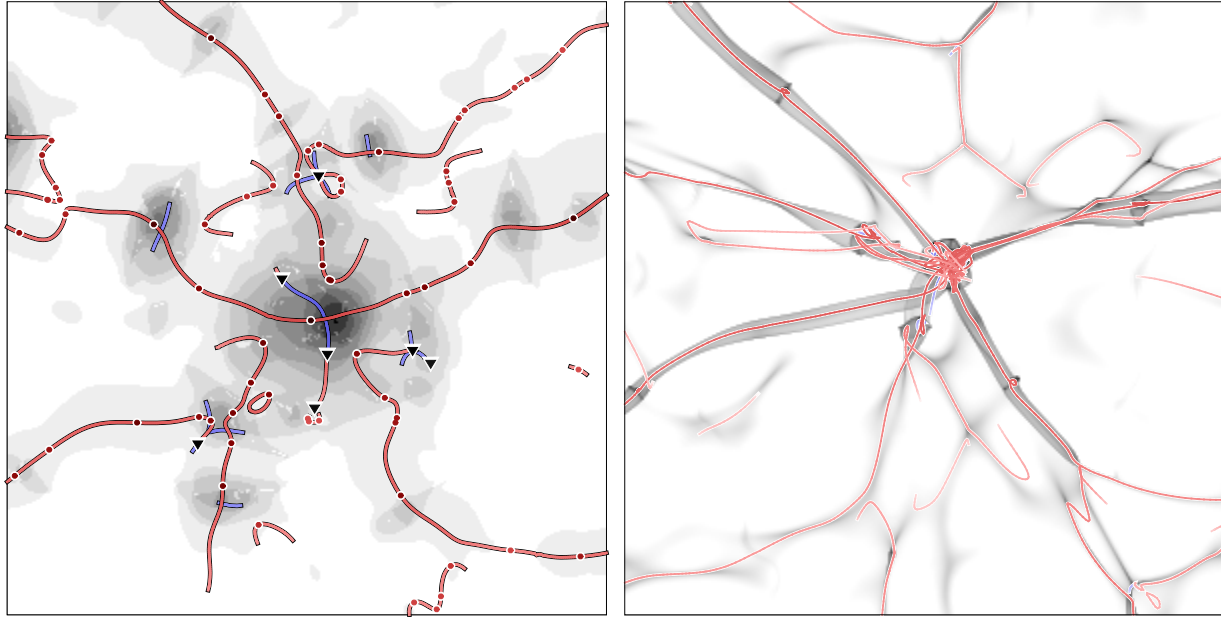


**Figure 16.** Relating singularities and singularity lines to N-body mass distribution. Left panel: the flip-flop field in Lagrangian space is shown by gray filled contours.  $A_3$  lines are shown by red lines. Points on  $A_3$  lines mark the extrema of the  $\lambda_1$  field. Triangles mark  $D_4$  points. Right panel: the structure formed at the nonlinear stage in 2D N-body simulation is shown in gray in Eulerian space. The  $A_3$  shown in the left panel are mapped to Eulerian space using the displacement field obtained in the N-body simulation.

the full 6-dimensional phase space structure of the cosmic mass distribution. Instead of following the mass distribution by means of a discrete number of particles, it follows the development of spatially extended mass elements.

Initially, the mass cells define a space-filling spatial tessellation, which is the tiling of Lagrangian space. The subsequent gravitational evolution is not only followed on the basis of the displacement of the cells but also on the basis of their deformation. Deformed cells of the evolving tessellation start to overlap as matter streams in the evolving mass distribution start to cross. At any one location in Eulerian space, one may determine at each epoch the number of overlapping cells as a direct reflection of the number of streams.

Alternatively, one may assume the Lagrangian view and determine the number of flips of parity experienced by mass cells. As they get deformed to the stage at which the cells pass through a singularity, they undergo a flip. The front- and backside of the cells get interchanged. The number of flips that the cells undergo corresponds directly to the number of times the corresponding mass element has been passing through a singularity. In turn, this directly reflects the number of resulting streams (Shandarin & Hidding 2013). For example, mass elements that have experienced singular collapse only once form the inner stream of pancakes.

As a means of connecting the dynamical state of evolution to the primordial mass distribution, our analysis follows the number of flips of mass cells and relates this to the number of times the mass element has been passing through a singularity. By following the number of parity

flips over time, we count the number of times a mass element passes through a fold. This *fold* field is discrete, given the number of singular collapses can only be discrete. The morphology of the fold field is similar to the ORIGAMI formalism and the concept of parity fields introduced by Neyrinck (2012). The major differences with ORIGAMI and parity fields is that the flip-flop field values are not limited to two - as in the case of parity fields - or to three - as in the ORIGAMI formalism. Also, we should point out that ORIGAMI is based on a different computational technique.

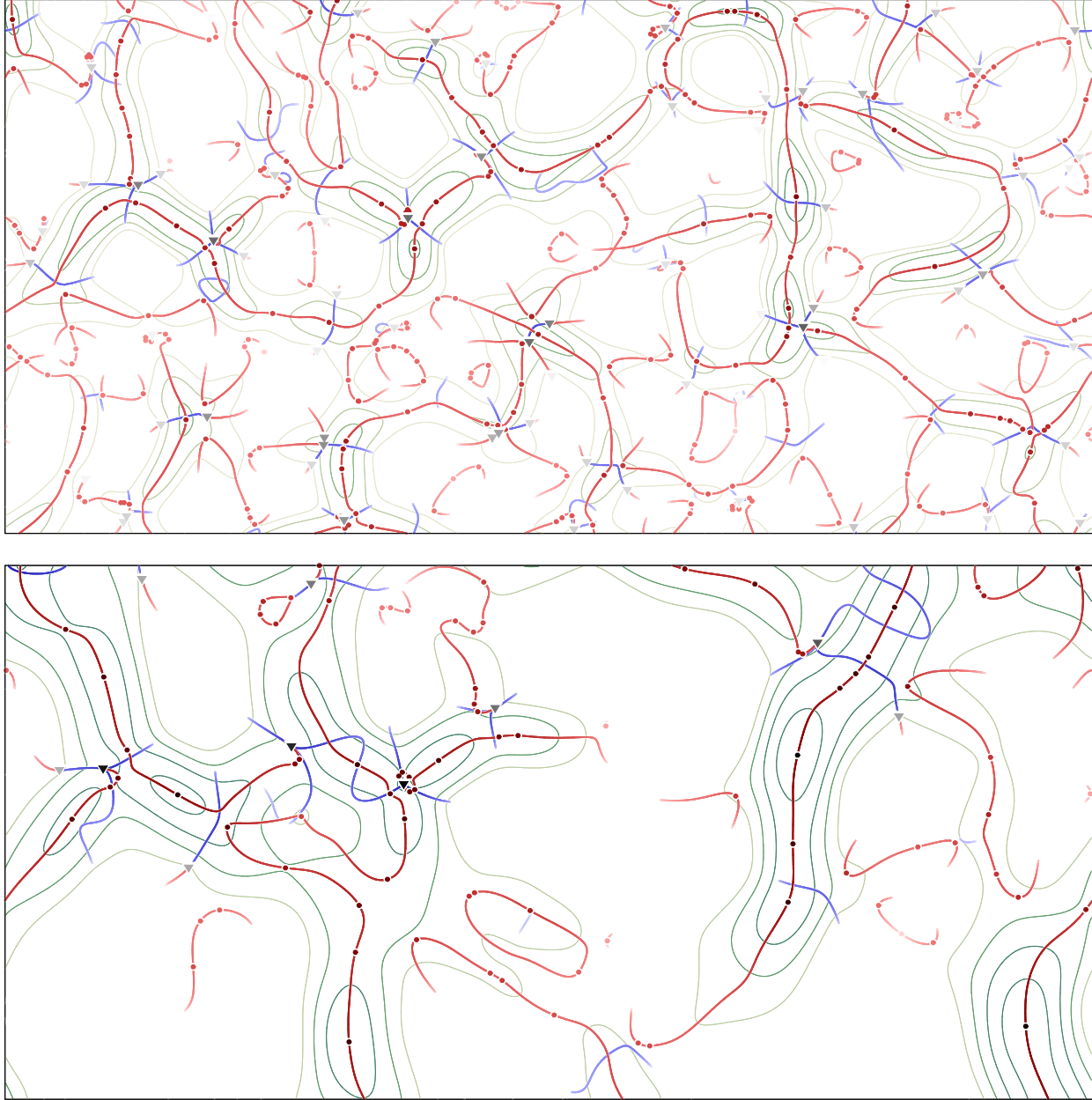
### 5.5.2 Case Study

Figure 16 makes a comparison between the Lagrangian constellation around a primordial density peak and the resulting nonlinear mass distribution in Eulerian space.

The central peak in the Lagrangian image (lefthand panel) depicts the major progenitor of the halo. The greyscale field represents the flip-flop field, with darker shades corresponding to a higher number of flip-flops and white representing the areas that still did not experience a state of singularity. The lightest shade of grey, to be found in the outer parts of the central halo and its nearby neighbouring regions, indicates the mass elements that have passed through a singularity only once.

Superimposed on the greyscale image are the thick solid red lines that indicate the  $A_3$  lines connecting to the peak and the ones that are to be found in its surroundings. Seven major  $A_3$  lines are seen to exit from the





**Figure 17.** Singularity structure as function of power spectrum.  $A_3$ -lines for two different powerspectra,  $P(k) = k^n$ ,  $k = 4$  (top),  $k = -1$  (bottom) both smoothed at the same scale. As expected for power spectra with a positive index, the pattern is much more regular. What is even more interesting is that the clustering statistics of the singularities seem to change in a non-trivial way. This will be the topic of a follow-up paper.

central peak. In the Lagrangian plane, the  $A_3$  lines pass through progenitors of other halos that merged with the central halo. In Lagrangian space, two of the  $A_3$  lines are connected at the center, while the remaining five are disconnected. While not connected in Lagrangian space, they will get intertwined through  $A_4$  singularities as they are mapped to Eulerian space (sect. 5.1 and sect. 5.3).

In the Eulerian image (righthand panel), the central

halo very much resembles a "knitting ball". This is an immediate consequence of the multiple collapses of the mass elements making up the halo, and is a reflection of this process being directed by the  $A_3$  lines.

Surrounding the halo, we find six pancakes - of a variety of lengths - connecting to the central halo. Overall, we may recognize and identify the various pancakes with the set of  $A_3$  lines. These appear to form a reasonably

good skeleton for the structure that we see emerging in Eulerian space. The pancake in the upper righthand part of the panel is the result of a merger of two pancakes, each corresponding to a different  $A_3$  line in the same region of the Lagrangian plane. The bifurcation of the  $A_3$  line is clearly standing out, and reflects the fact that the merger of the pancakes has not yet been completed,

### 5.6 Perturbation Power Spectrum and Skeleton Singularity Structure

Having obtained insight into the identity, location, connections and role of singularities in the buildup of the cosmic web, we may turn towards the issue of the dependence of the spatial configuration of  $A_3$  lines and the related singularities on the cosmological scenario.

There have not been many systematic studies that address the dependence of the cosmic web characteristics on the underlying cosmology. The one exception are several recent studies that have looked at the properties of voids as probes of the nature of dark matter (Hellwing et al. 2010; Li 2011) and the nature of dark energy (Park & Lee 2007; Lavaux & Wandelt 2010, 2012; Bos et al. 2012). One of the problems for using filaments and walls as probes for the cosmology, is our still existing lack of a real quantitative understanding of their structure and connectivity.

In this study we have demonstrated that most of the structure of the cosmic web can be condensed in terms of well established and defined mathematical concepts,  $A_2$  and  $A_3$  lines and the classes of  $A$ - and  $D$ - singularities. In an follow-up publication we will present a detailed and systematic study of the spatial distribution of singularities and  $A_2$  and  $A_3$  lines as a function of the underlying cosmology. Here we provide a quick impression of what we may expect.

A good impression of the high sensitivity of the cosmic web singularity structure in two different cosmologies can be obtained from figure 17. It shows the location of  $A_3$  lines and  $\alpha$  eigenvalue contours, along with the corresponding singularity points, for two realizations of the mass distribution in the Lagrangian plane. The top panel concerns the pattern for a scenario with a  $P(k) \propto k^4$  power law power spectrum, dominated by high frequency components, and one with a much more large scale character,  $P(k) \propto k^{-1}$ . Both realizations have been smoothed on the same scale.

The spine in the  $P(k) \propto k^{-1}$  cosmology (lower panel) is dominated by some very long and stretched  $A_3$  lines. The weblike pattern in the  $P(k) \propto k^4$  cosmology seems to have a much more unordered complexion. The cosmic web in that scenario is assembled out of many short  $A_3$  lines. Still, it has a clearly outlined cellular structure, in which the  $A_3$  lines appear to loop around areas of low  $\alpha$  values (usually low density areas).

In summary, we may conclude that the description of the Lagrangian field structure in terms of singularity lines and points is a very promising and potentially powerful

way of exploiting the cosmological information content of the cosmic web.

## 6 THE THIRD DIMENSION

Following the extensive two-dimensional analysis described in the previous sections, we need to discuss how it relates to the structure we find in the fully three-dimensional world. While a comparable fully detailed analysis of the three-dimensional singularity structure in the Zel'dovich approximation will be the subject of a separate upcoming publication, we here discuss some relevant observations. These pertain mostly to the relevance of the 2D discussion to the three-dimensional situation.

It may not come as a surprise that the three-dimensional singularity structure of the patterns generated via the Zeldovich approximation is considerably more complex than in the two-dimensional situation. Nonetheless, the detailed assessment of the two-dimensional singularity structures presented in this study includes several important and relevant aspects that can be directly related to the equivalent three-dimensional situation.

A range of key observations on singularities, caustics and catastrophes in 3D may be made. In the following, we shortly discuss the most important ones.

### 6.1 Caustic Families

In the two-dimensional situation, the 2 eigenvalues of the deformation tensor field express themselves in the existence of two families of caustics, the  $\alpha$ - and  $\beta$ -caustics. Given the three eigenvalues of the corresponding deformation tensor in 3D, there are three families of caustics, the  $\alpha$ -,  $\beta$ - and  $\gamma$ -caustics.

On the basis of the corresponding transformation, the global geometry and topology of the cosmic web in three dimensions is determined by the set of  $A_3^\alpha$ -surfaces. Other singularities live on the set of  $A_3^\alpha$ -surfaces. They are the equivalent of the set of  $A_3^\alpha$ -lines, and  $A_3^\beta$ -lines, that we found in this study as the features that define the spine of the cosmic web.

### 6.2 2D singularities and their 3D equivalents

For those 3D singularities that have an equivalent singularity in 2D, we find - taking into account trivial generalizations - that the structure of the caustics remain largely equivalent. One particular aspect for which this is always true is the density profile near singularities. These turn out to remain the same for equivalent singularities in different dimensions.

A particular example is that of the simplest caustic, the  $A_2$ . In 1D, the  $A_2$  caustic is a point and in 2D it is a line. In the equivalent three-dimensional situation, it is a surface. As was pointed out above, the  $A_2$  caustic retains

Family	type	name	Eulerian dimension
A-series	$A_2$	fold	surface
	$A_3$	cusps	curve
	$A_4$	swallow-tail	point
	$A_5$	butterfly	transient
D-series	$D_4^-$	elliptic umbilic (purse)	point
	$D_4^+$	hyperbolic umbilic (pyramid)	point
	$D_5$	parabolic umbilic	transient

**Table 3.** Inventory of 3D singularity classes.

the same density profile near the singularity as in two dimensions,  $\rho(r) \propto r^{-1/2}$ .

The other type of singularity which also exists in 1D is the  $A_3$  singularity. In one-dimensional space  $A_3$  singularities are located at a specific set of singular points. At these points, they will only exist as singularity at one particular instant of time. In two dimensions, they are located on  $A_3$  lines and at any one instant materialize as *cusps* at isolated points along those lines. In three-dimensional space, they are located on surfaces and at any specific instant they materialize on a set of lines. In both 1D, 2D and 3D, the mean density profile of these singularities is the same,  $\rho(r) \propto r^{-2/3}$ .

### 6.3 New singularities

In addition to the classes of singularities that we could also identify in the two-dimensional situation, there are new types of singularities in the 3D situation. The emergence of new types of singularities in higher dimensional situations is not unexpected. For instance, the  $A_4$  and  $D_4$  singularities that we found in this 2D study do not exist in 1D.

In three dimensions, the list of singularity classes is extended by that of  $A_5$  and  $D_5$  singularities. They are the only new singularities emerging in the three-dimensional situation. The  $A_5$  and  $D_5$  singularities have a considerably more complex structure than the singularities which have two-dimensional equivalents. This is not unlike the substantially more complex structure of the  $A_4$  and  $D_4$  singularities with respect to the structure of the  $A_2$  and  $A_3$  singularities. The latter exist also in 1D and have a more basic geometry.

### 6.4 A and D singularities: 2D versus 3D

In the previous sections we had observed that there is a principal difference between *A*- and *D* singularities. While the *A*-singularities are determined by only one deformation tensor eigenvalue, *D* singularities are determined by the values of two eigenvalues. Note that this also implies that *D*-singularities cannot exist in one-dimensional space.

In three-dimensional space, up to three eigenvalues may be involved in determining a singularity. In principle

one might therefore expect the existence of an additional new class of singularities. This turns out not to be the case. There is no additional new singularity class, with the exception of the trivial case of  $D_{\beta=\gamma}$ -singularities. These have exactly the same topology as  $D_{\alpha=\beta}$ -singularities.

The reason that there are no additional singularities of a new type is quite straightforward. In a generic deformation field in 3D there are no points where  $\alpha = \beta = \gamma$ .

### 6.5 The three-dimensional singularity inventory

To summarize, in table 3 we list the full inventory of catastrophes that exist in 3D space.

Also in three-dimensional space it is possible to extract a skeleton of surfaces, lines and nodes on the basis of a singularity analysis equivalent to the one discussed for the two-dimensional situation.

Filamentary structures are traced by swallow-tail caustics, as well as by  $D_4$  umbilics. From the experience in the two-dimensional situation, we know that umbilics are never far from a swallow-tail. However, the inverse need not be true: there are swallow-tails that emerge without any umbilic in their vicinity. Given the fact that the 2D case is to some extent a section of the 3D situation, the same is still true in three dimensions.

From this, we may conclude that in three dimensions filaments will have a diversity of morphologies, each marked by a highly complex structure.

### 6.6 Singularities in 2D and 3D: differences

An illustration of three dimensional structure predicted by the the ZA in 3D is shown in figure 18. The caustic surfaces are computed using the tessellation of the Lagrangian submanifold and subsequently projected to Eulerian space, following the description by Shandarin, Habib & Heitmann (2012). The resulting figure is a three-dimensional analogy of the top right panel of figure 1, including the  $\beta$ -caustics shown in red.

Comparing the characteristic weblike structure in figure 18 with that obtained by topological techniques for the dissection of the cosmic mass distribution on the basis of the watershed transform (Platen et al. 2007). Telling examples for related results are those that are obtained by the spineweb technique of Aragón-Calvo et al. (2010) and

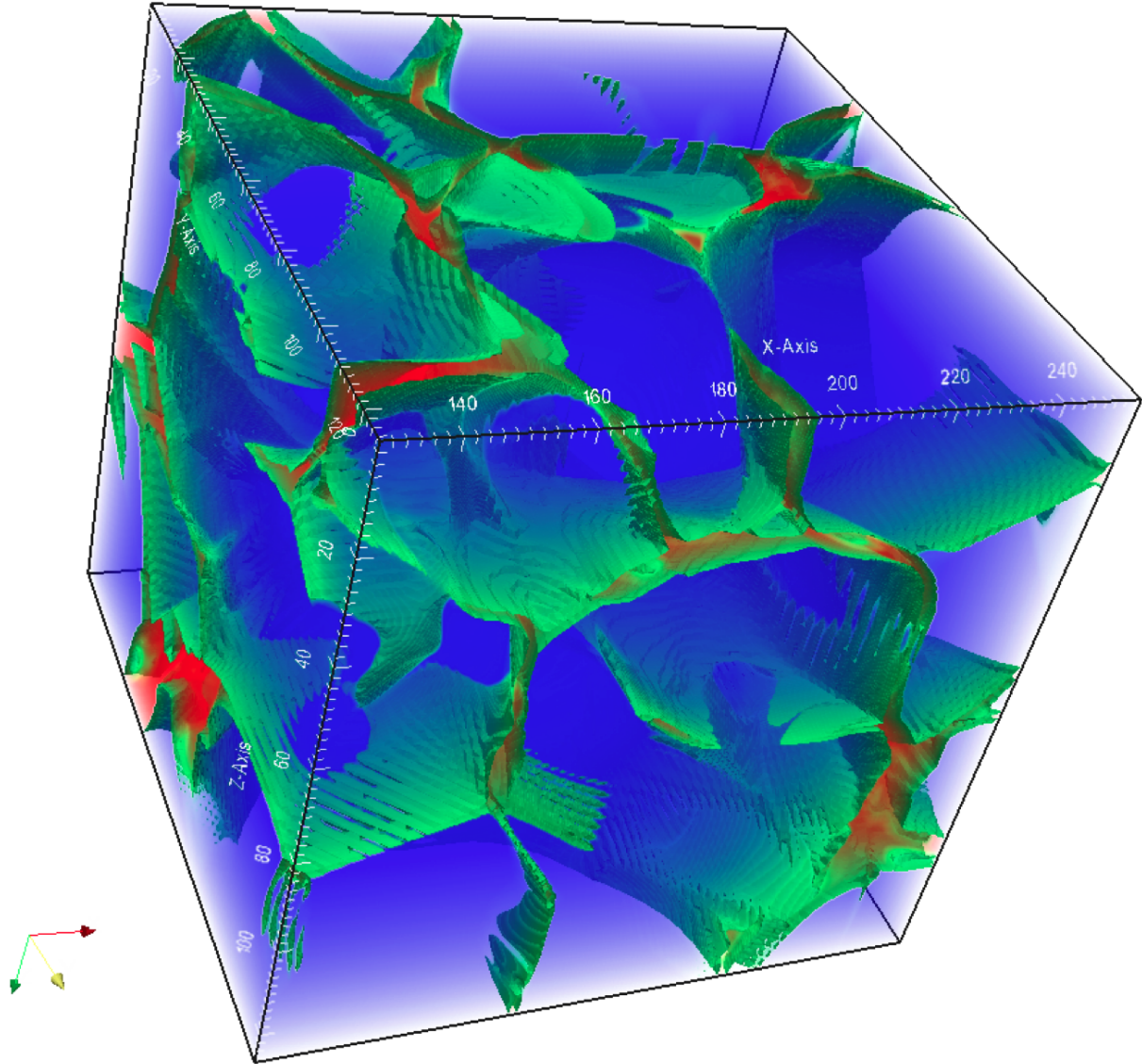


**Figure 18.** Caustic structure of ZA evolved mass distribution in 3D. This is a three-dimensional analogy of the top right panel in figure 1. The  $\alpha$ -caustics are shown in green and  $\beta$ -caustics in red. The  $\beta$ -caustics are seen only through the openings in the surface of  $\alpha$ -caustics by the box faces. This is the reason why one cannot see  $\gamma$ -caustics.

the skeleton technique described in Sousbie et al. (2009). Also other methods for the dissection of the cosmic spatial mass distribution into its individual structure components, such as the multiscale morphology MMF/Nexus formalism (Aragón-Calvo et al. 2007; Cautun et al. 2013) and the tidal and shear tensor methods, advocated by Hahn et al. (2007); Forero et al. (2008) and Libeskind et al. (2012), produce spatial patterns that resemble the one seen in figure 18. For example, figure 8 in Aragón-Calvo et al. (2010) (also see fig. 15 in van de Weygaert et al. (2009)) and figure 4(a) in Sousbie et al. (2009) reveal a striking qualitative similarity of the weblike structure obtained by the topological spineweb and skeleton techniques and the

geometric singularity structure in the Zel'dovich approximation shown in figure 18.

In one sense, there is a profound link between topology-based pattern identification and the description of the dynamically evolving mass distribution in terms of its singularity structure. Both are intimately linked to Morse theory. In terms of the structural analysis of the cosmic mass distribution, Morse theory was first invoked by Colombi et al. (2000). They used it to characterize the structure of the primordial field of Gaussian density fluctuations. However, a complete characterization in terms of the full array of complex structural components seen in the observed pattern of the cosmic mass distribution

became only possible after Platen et al. (2007) had introduced the watershed transform.

The similarity between the topology-based identification of the components of the cosmic web and the structure encountered in the Zeldovich approximation demonstrates that the latter represent a viable framework for the analysis of N-body simulations. In particular, this concerns the relation between the initial density and potential field in Lagrangian space and the resulting web in Eulerian space.

We should emphasize that the topological structure identification advocated by Arag3n-Calvo et al. (2010) and Sousbie et al. (2009) is applied to the evolved matter distribution at a particular cosmic epoch. They are not dynamical descriptions that invoke the initial field of density fluctuations. Instead, they are more intent on connecting the outcome of N-body simulations to the structure seen in the observational reality.

Instead, when the analysis described in this paper is extended to its three-dimensional setting, it will provide a dynamical formalism for connecting the primordial Lagrangian density field to the weblike structure obtained in simulations. We expect that the combination of the topological structure identification methods and our dynamical formalisms will lead to a set-up in which observational structures can be more directly and significantly related to the initial cosmological conditions than hitherto possible with existing techniques.

## 7 SUMMARY & OUTLOOK

In this study, we have presented and extensively discussed a comprehensive geometric model for the formation of the caustic structure in the frame of Zeldovich approximation Zeldovich (1970); Shandarin & Zel'dovich (1989). Via the identification of singularities appearing in the evolving mass distribution, and by establishing the geometric nature of their connections, our model represents a direct analytical description of the dynamical origin of the spine of the cosmic web Bond, Kofman & Pogosyan (1996); van de Weygaert & Bond (2008).

In this study we have restricted ourselves to the two-dimensional equivalent of the full three-dimensional system. Because of the complexity of the mathematics involved, catastrophe theory of Lagrangian singularities, it is necessary to build an intuition for the relevant mathematical and physical context before one can embark on the considerably more complex three-dimensional situation. Moreover, although the two-dimensional case can not really be directly compared with the full three-dimensional structure of the cosmic web, it turns out to provide us with most of the concepts, principles and language that pertain in 3D space.

The Zeldovich approximation Zeldovich (1970); Shandarin & Zel'dovich (1989) has been demonstrated to be a good theoretical model for the evolution of cosmic structure into the mildly nonlinear regime of struc-

ture formation. It crudely, yet conceptually correctly, describes the onset of the non-perturbative quasi-linear regime. This includes the emergence of multistream flow regions and caustics (Doroshkevich, Ryabenkii & Shandarin 1973; Shandarin & Zel'dovich 1989; Buchert 1989, 1992; Coles, Melott & Shandarin 1993; Melott, Pellman & Shandarin 1994; Melott, Shandarin & Weinberg 1994; Coles & Sahni 1995; Melott, Buchert & Weiss 1995; Yoshisato, Matsubara & Morikawa 1998; Yoshisato, et al. 2006). Its main virtue is that of a good approximate description of structures on scales larger than the scale of nonlinearity, while erasing structures on smaller scales. In the currently popular hierarchical scenarios of structure formation, such as the  $\Lambda$ CDM standard cosmology, small scale structure does not heavily influence the structure that emerges on larger scales (see e.g. Little, Weinberg & Park 1994). This implies the Zel'dovich approximation to remain a reasonably good description for the large scale Universe.

We have put the Zeldovich approximation into the geometric framework used in the mathematical theory of singularities and catastrophes (Thom 1969; Zeeman 1977; Arnold 1982, 1983). Our analysis is directed towards understanding the structure and projections of the Lagrangian submanifold, the four-dimensional phase-space  $(\mathbf{q}, \mathbf{x})$ . From catastrophe theory, it is known that there are only a limited number of different singularity classes. We commence our study with a systematic identification of these singularities. We follow the well-known ADE classification of catastrophes introduced by Arnold, yielding the cryptic notation of  $A_2$  singularities for *fold* singularities, the  $A_3$  *cusp* singularities, the  $A_4$  *swallow-tail* singularity and the  $D_4$  *umbilic* singularities. Central in this characterization is the analysis of the Lagrangian spatial structure of the two fields of eigenvalues  $\alpha$  and  $\beta$  of the deformation tensor that characterizes the displacement field in the Zeldovich approximation. We study the singularities in Lagrangian space, in their identity as the progenitors of caustics in Eulerian space. We combine this with an assessment of the corresponding evolution of the Eulerian environment of the emerging caustics.

A crucial and fundamental singularity is the  $A_2$  *fold* singularity, which is the progenitor of the well-known *pancake* that has become one of the most familiar features in the structure that we see emerge in Zeldovich descriptions of the evolving cosmic mass distribution. In addition, we provide an impression of the additional point-like singularities -  $A_3^+$ ,  $A_3^-$ ,  $A_4$ ,  $D_4^+$  and  $D_4^-$  - on the basis of illustrations of three-dimensional projections of the corresponding phase-space manifolds. Crucial in the dynamical context that we are considering is that they are stable under perturbation. This implies that they remain in existence, in one form or the other, into the nonlinear regime of gravitational instability.

The key finding of our study is that in Lagrangian space all point-like singularities -  $A_3^+$ ,  $A_3^-$ ,  $A_4$ ,  $D_4^+$  and  $D_4^-$  - are located on characteristic one-dimensional lines, the  $A_3$ -lines. In Lagrangian space, the outline of these lines is

defined by the fundamental structure equation 18. This definition is entirely motivated by the dynamics of the Zeldovich Approximation.

The  $A_3$  lines delineate the sites where all dynamical activities involved in the buildup of the cosmic web are taking place. They form the site around which we find the emergence and merger of pancakes, the bifurcation of cusps in Eulerian space, and the merger of caustics. The most complex dynamical processes take place at the crossings of pancakes. These usually involve singularities of different types and usually are the places where most halos are formed. It is worth stressing that the collapse is highly non-spherical. This is true for intersections of pancakes and for regions around  $D_4$  singularities, where  $\alpha = \beta$ .

When mapped to Eulerian space the  $A_3$  lines outline the spine of the cosmic web. In essence, as the structure equation 18 only involves quantities at one point it represents a local definition of the skeleton of the cosmic web. Geometrically it can be defined either as a set of points where the gradient of one of the eigenvalues is orthogonal to the corresponding eigen vector or, equivalently, as a set of points where the eigen vector is tangential to the level contour of the corresponding eigen value.

In summary, we find that the complex geometry of cosmic structure can be understood to a large extent by the  $\alpha$ -fields of the principal eigenvalue  $\alpha$  of the deformation tensor, and through these specifically through the outline of the  $A_3^\alpha$ -lines. The role of  $\beta$  field is considerably more modest. This is largely due to the fact that the first collapse of mass elements is directed towards  $A_3^\alpha$ -lines. The  $A_3^\beta$ -lines tend to bend and wrap around  $A_3^\alpha$ -lines. Nonetheless, locally the  $A_3^\beta$ -lines play a significant role in the highest concentrations of mass, ie. the locations where halos form.

In this study, we have also made a beginning with the comparison of the spinal structure outlined by our geometric description and that found in fully nonlinear two-dimensional N-body simulations. By identifying the  $A_3$  lines in the (Lagrangian) displacement field of the 3D N-body simulations, and mapping them to Eulerian space we can compare the resulting network with the cosmic web skeleton that emerged in the simulation. We find that it indeed encapsulates quite an accurate skeleton of the cosmic web.

As yet, we do not present a statistical study of the two-dimensional case. One of the reasons is that the structure in three dimensions will differ significantly from that in two dimensions. We therefore refer such a study to the upcoming extension of our analysis to three dimensions. A more extended comparison with cosmological N-body simulations is also referred to such a 3D study.

This study has paved the road towards a profound dynamical analysis of the detailed and intricate structural aspects of the cosmic web. We expect that its combination with the outcome of large N-body simulations will help us towards a considerable improvement of our understanding of the processes involved in the buildup of structure, not

only limited to the highly nonlinear formation and virialization of fully collapsed dark halos but also that of the prominent filamentary features that appear to dominate the maps produced by large galaxy surveys.

## ACKNOWLEDGMENTS

We gratefully acknowledge numerous helpful and inspiring discussions with Bernard Jones and Gert Vegter. S. Shandarin and R. van de Weygaert acknowledge the support from the New Frontiers of Astronomy and Cosmology program at the Sir John Templeton Foundation. S. Shandarin and R. van de Weygaert also acknowledge the support by the NWO visitor program (grant #040.11.344). In addition, S. Shandarin acknowledges the scholar visitor program at ANL where the text of the paper was finalized.

## REFERENCES

- Abel, T., Hahn, O., & Kaehler, R. 2012, MNRAS, 427, 61
- Aragón-Calvo M.A., Jones B. J. T., van de Weygaert R., van der Hulst J. M., 2007, Astron. Astrophys., 474, 315
- Aragón-Calvo M.A., Platen E., van de Weygaert R., Szalay A.S., 2010, Astrophys. J., 723, 364
- Arnold V.I., 1982, Trudy Seminara imeni I.G. Petrovskogo, 8, 21
- Arnold V.I., 1983, Uspekhi Mat. Nauk 38, 77
- Arnold V.I., 1992, Catastrophe Theory, 3rd ed., Springer-Verlag
- Arnold V.I., Shandarin S.F., Zel'dovich Ya.B, 1982, Geophysical and Astrophysical Fluid Dynamics, 20, 111
- Bardeen J.M., Bond J.R., Kaiser N., Szalay A., 1986, ApJ, 304, 15
- Bond J.R., Kofman L., Pogosyan D., 1996, Nat, 380, 603
- Bond J.R., Myers S.T., 1996a, ApJS, 103, 1
- Bond J.R., Myers S.T., 1996b, ApJS, 103, 41
- Bond J.R., Myers S.T., 1996c, ApJS, 103, 63
- Bos E.G.P., van de Weygaert R., Dolag K., Pettorino V., 2012, MNRAS, 426, 440
- Buchert T., 1989, Astron. Astrophys., 223, 9
- Buchert T., 1992, MNRAS, 254, 729
- Cautun M., van de Weygaert R., Jones B. J. T., 2013, MNRAS, 429, 1286
- Coles P., Sahni V., 1995, Physics Reports, 262, 1
- Coles P., Melott A.L., Shandarin S.F., 1993, MNRAS, 260, 765
- Colombi S., Pogosyan D., Souradeep T., 2000, Phys. Rev. L., 85, 5515
- Doroshkevich A., 1970, Astrophysics, 6, 320
- Doroshkevich A.G., Shandarin S.F., 1973, Astrophysics, 9, 332
- Doroshkevich A.G., Ryabenskii V.S., Shandarin S.F., 1973, Astrophysics, 9, 144



- Doroshkevich A.G., Kotok E.V., Novikov I.D., Polyudov A.N., Shandarin S.F., Sigov Yu.S., 1980, MNRAS, 192, 321
- Falck, B. L., Neyrinck, M. C., & Szalay, A. S. 2012, ApJ, 754, 126
- Forero-Romero J.E., Hoffman Y., Gottlöber S., Klypin A., Yepes G., 2008, MNRAS, 396, 1815
- Gurbatov S.N., Saichev A.I., Shandarin S.F., 1989, MNRAS, 236, 385
- Gurbatov S.N., Saichev A.I., Shandarin S.F., 2012, Physics - Uspekhi, 55, 223
- Hahn O., Porciani C., Carollo C. M., Dekel A., 2007, MNRAS, 375, 489
- Hellwing W.A., Juszkiewicz R., van de Weygaert R., 2010, Phys. Rev. D., 82, 3536
- Hidding J., van de Weygaert R., Vegter G., 2013, MNRAS, to be subm.
- Icke V., 1972, Formation of Galaxies Inside Clusters, Ph.D. thesis, Leiden University
- Icke V., 1973, A&A, 27, 1
- Klypin A.A., Shandarin S.F., 1983, MNRAS, 204, 891
- Kofman L., Pogosyan D., Shandarin S., 1990, MNRAS, 242, 200
- Lavaux G., Wandelt B.D., 2010, MNRAS, 403, 1392
- Lavaux G., Wandelt B.D., 2012, Astrophys. J., 754, 109
- Li B., 2011, MNRAS, 411, 2615
- Libeskind N.I., Hoffman Y., Knebe A., Steinmetz M., Gottlöber S., Metuki O., Yepes G., 2012, MNRAS, L137
- Lin C.C., Mestel L., Shu F.H., 1965, Astrophys. J., 142, 1431
- Little B., Weinberg D.H., Park C., 1991, MNRAS, 253, 295
- Melott A.L., Pellman, T.F., Shandarin S.F., 1994, MNRAS, 269, 638
- Melott A.L., Buchert T., Weiss 1995, A&A, 294, 345
- Melott A.L., Shandarin S.F., Weinberg D., 1994, Astrophys J, 428, 28
- Milnor J.W., 1963, Morse Theory, Ann. Math. Stud., 51, Princeton Univ. Press
- Neyrinck, M.C., 2012, MNRAS, 427, 494
- Novikov D., Colombi S., Doré, 2006, MNRAS, 366 1201
- Park D., Lee J., 2007, Phys Rev. L., 98, 1301
- Peebles J.P.E., 1980, The Large-Scale Structure of the Universe
- Platen E., van de Weygaert R., Jones B. J. T., 2007, MNRAS, 380, 551
- Pogosyan D., Pichon C., Gay C., Prunet S., Cardoso J.F., Sousbie T., Colombi S., 2009, MNRAS, 396, 635
- Rozhanskii L.B., Shandarin S.F., 1984, preprint No. 79, Inst. of Appl. Math., Akad. of Sci. USSR, Moscow
- Shandarin, S. F. 2011, JCAP, 5, 15
- Shandarin S.F., Hidding 2013, in preparation
- Shandarin S.F., Zel'dovich Ya.B. 1989, Reviews of Modern Physics, 61, 185
- Shandarin S., Habib S., Heitmann K., 2012, Phys. Rev. D, 85, 083005
- Sousbie T., Pichon C., Colombi S., Novikov D., Pogosyan D., 2008, MNRAS, 383, 1655
- Sousbie T., Colombi S., Pichon C., 2009, MNRAS, 393, 457
- Thom R., 1969, Topology, 8, 313
- Thom R., 1972, Structural Stability and Morphogenesis, W.A. Benjamin
- Tremaine, S. 1999, MNRAS, 307, 877
- Tricoche X., 2002, Vector and Tensor Topology Simplification, Tracking, and Visualization, PhD thesis, Univ. Kaiserslautern
- van de Weygaert R., Aragón-Calvo M.A., Jones B.J.T., Platen E., 2009, IEEE CPS, E3781, 3-31
- van de Weygaert R., Bond J.R., 2008, LNP, 740, 335
- Vasiljev V.A., 1977, Func. Anal. Appl. 11, 5
- White S.D.M., Silk J., 1979, Astrophys.J., 231, 1
- Yosisato A., Matsubara T., Morikawa M., 1998, ApJ, 498, 48
- Yosisato A., Morikawa M., Gouda N., Mouri H., 2006, ApJ, 637, 555
- Zeeman E.C., 1977, Catastrophe theory. Selected papers 1972-1977, AddisonWesley
- Zel'dovich Ya.B., 1970, A&A 5, 84
- Zel'dovich Ya.B., Mamaev A.V., Shandarin S.F. 1983, Sov. Phys. Usp. 26,77

#### APPENDIX A: LAGRANGIAN SUBMANIFOLD IN ONE-DIMENSIONAL CASE

The middle panel in the top row of figure A shows the Lagrangian submanifold embedded in a two-dimensional space where the horizontal axis is Lagrangian coordinate  $q$  and the vertical axis is Eulerian coordinate  $x$ . Three curves show three qualitatively different states of the evolution of a sinusoidal perturbation. The red diagonal line shows the initial state when  $x = q$ , the green line shows the instant of the origin of  $A_3$  singularity at the origin. Finally, the blue line shows the state with three streams between two singularities of  $A_2$  type. Three panels surrounding the central panel shows the initial velocity  $\propto s(q)$  (the bottom panel), the evolution of the phase space (the left panel) and the density field in Eulerian space (the right panel). Three density fields are the projections of either the phase-space lines from the left panel or the Lagrangian submanifolds from the central panel on Eulerian coordinate  $x$  at the corresponding times. The information content of the phase-space and the Lagrangian submanifold is similar but it is greater than that of the density field. Singularities do exist neither in the phase space nor in the Lagrangian submanifold, they emerge as a result of the projection to Eulerian space only. The caustics are located at the points where the projecting direction is tangent to the phase-space curve or the Lagrangian submanifold. All geometrical features just described are similar in two and three dimensions. The major difficulty is due to complexity of projection the Lagrangian submanifolds from four- or six-dimensional spaces to two-

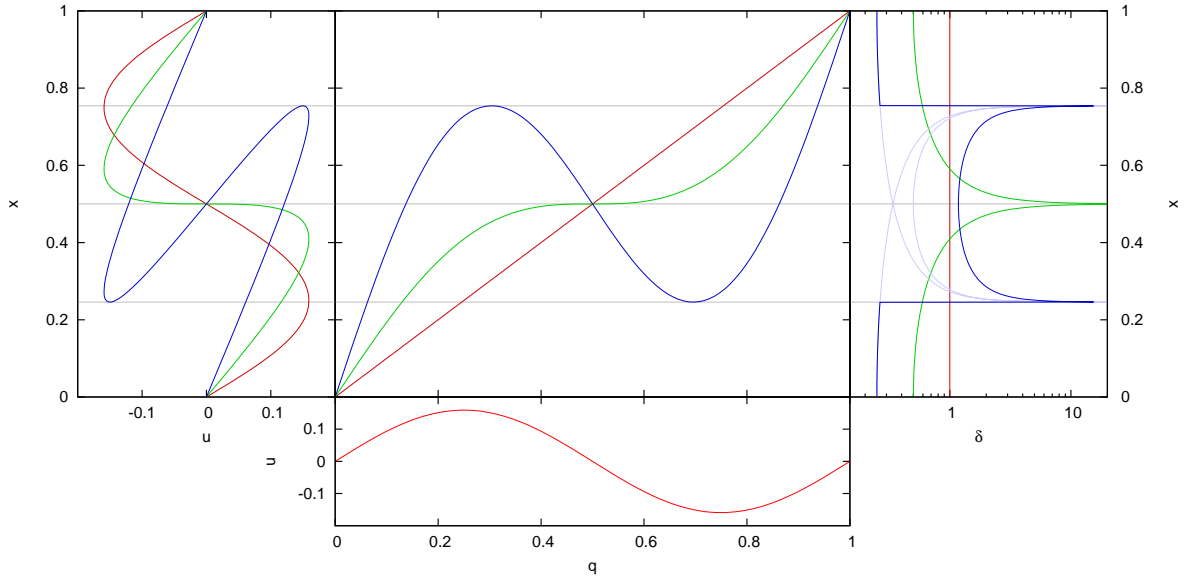


**Figure A1.** One-dimensional phase-space manifold evolution. The evolution of singularities in the most simple one-dimensional example of the ZA, a sinusoidal perturbation. In this case we find a single transient  $A_3$  cusp singularity (black line), immediately followed by two  $A_2$  folds (blue lines). Centre panel: Lagrangian  $(q, x)$  manifold at three subsequent timesteps. Left panel: velocity streams, i.e. velocity as function of Eulerian position  $x$ , around Eulerian catastrophe. Right panel: density structure  $\delta(x)$  around Eulerian catastrophe. Bottom panel: velocity  $u$  of Lagrangian mass elements  $q$ .

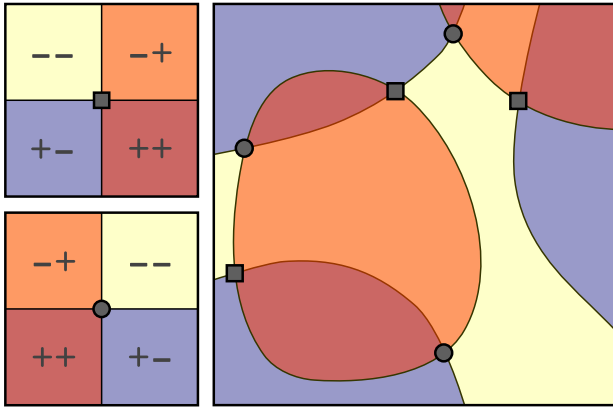


**Figure B1.** The two different geometries of  $D_4$  singularities are in the space of  $d_{11} - d_{22}$  and  $d_{12}$  each others mirrors. This illustration shows why topologically there must always be as many  $D_4^-$  as  $D_4^+$  singularities.

or three-dimensional Eulerian spaces respectively. As a result the number of archetypical singularities increases with the growth of the number of dimensions.

## APPENDIX B: ABOUT LOOPS NEAR $D_4^-$ SINGULARITIES.

The small loops near  $D_4^-$  singularities form a salient feature in our results. In this appendix we show how this result can be understood in terms of the higher order  $D_5$  catastrophe. The  $D_5$  catastrophe in 3-D marks the transition from a  $D_4^-$  to  $D_4^+$  catastrophe. As we mentioned before the  $D_4$  singularity is a location where both eigenvalues are equal, and we derived the following equation from the deformation tensor  $d_{ij}$ , that if  $\alpha(\mathbf{q}) = \beta(\mathbf{q})$ , then

$$d_{11} = d_{22} \quad \text{and} \quad d_{12} = 0. \quad (\text{B1})$$

To determine the type we had to look at the higher derivatives of the potential.

Formally the amount of  $D_4^+$  and  $D_4^-$  singularities are exactly equal. This can be seen from the topology of the method by which we find them. The two fields  $U_1 = d_{11} - d_{22}$  and  $U_2 = d_{12}$  are Gaussian and uncorrelated. The zero-levelset is the boundary between regions that are negative and positive. A point where both fields are zero exists then in two kinds, illustrated in figure B1. In practice, some of these points have a corresponding eigenvalue that is negative, so these points are not considered in our figures.

A  $D_5$  singularity corresponds to the situation where



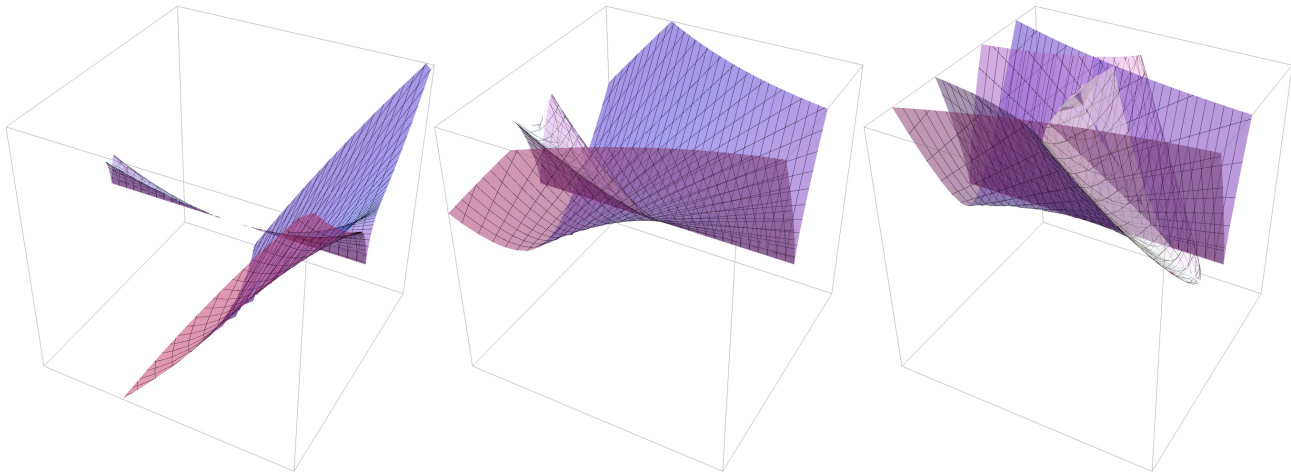


**Figure B2.** The  $D_5$  catastrophe. Here we plotted the caustic surface of the catastrophe in 3d. To interpret its significance in 2d, we need to take a cross-section of this image, moving in time from the front-right plane to the left-back or vice versa. In this sense each of these three images shows an evolution history of caustics in 2d. The 3d evolution shows us how this evolution might change if we smoothly change some parameter determining the character of the 2d field. For example by slowly changing some of the phases in a random realisation of the potential, we can change a  $D_4^-$  on the left into a  $D_4^+$  on the right.

the zero-sets of  $U_1$  and  $U_2$  touch exactly<sup>5</sup>. In general this never happens, however the probability that a  $D_4$  point is *close* to that, is very high. This means that the global geometry of a  $D_4^-$  tends to look a lot like that of a  $D_5$  singularity.

If we now look at figure B2, we can see what a geometry close to a  $D_5$  looks like. In the first of the three images, if we take an intersection and move it from right to left, we start with a single cusp. This cusp is then joined by two swallowtails, to form a triangle of cusps. This triangle contracts to a  $D_4^-$ , and then expands again as a triangle of cusps in the second eigenvalue. By the same recipe we can approach the  $D_4^+$  catastrophe, seen in the right-most panel in figure B2. We start out with an  $\alpha$ -cusp. This cusp is joined by a  $\beta$ -pancake, which is soon thereafter pierced by the  $\alpha$ -cusp. The cusp “changes colour” and through the  $D_4^+$  becomes a  $\beta$ -cusp. Both these scenarios are frequently encountered in the ZA, even if they don’t result in an eventual  $D_4$  singularity, as is evident from figures 9, 10, 11, 13 and 14.

This paper has been typeset from a T<sub>E</sub>X/L<sup>A</sup>T<sub>E</sub>X file prepared by the author.

<sup>5</sup> In the language of geometry, to have a stable configuration, the sets must cross *transversally*.